Journal of Electron Spectroscopy and Related Phenomena 241 (2020) 146883

Contents lists available at ScienceDirect

Journal of Electron Spectroscopy and Related Phenomena

journal homepage: www.elsevier.com/locate/elspec

Secondary electron generation mechanisms in carbon allotropes at low impact electron energies

Alessandra Bellissimo[a,c,*], Gian Marco Pierantozzi[a], Alessandro Ruocco[a], Giovanni Stefani[a], Olga Yu. Ridzel[b], Vytautas Astašauskas[b], Wolfgang S.M. Werner[b], Mauro Taborelli[c]

[a] Dipartimento di Scienze, Università degli Studi Roma Tre, Via della Vasca Navale 84, I-00146 Rome, Italy
[b] Institut für Angewandte Physik, Vienna University of Technology, Wiedner Hauptstrasse 8-10, A 1040 Vienna, Austria
[c] CERN, European Organization for Nuclear Research, CH-1211 Geneva 23, Switzerland

ARTICLE INFO

Keywords:
Low-energy electrons
Electron-induced secondary electron emission
Electron pair spectroscopy
(e,2e)-coincidence spectroscopy
Plasmon excitation
Total electron yield
Carbon allotropes

ABSTRACT

More than a century after the discovery of the electron, there are still fundamental, yet unresolved, questions concerning the generation-ejection mechanism of the ubiquitous Secondary Electrons (SEs) from a solid surface. Broadness of the field of application for these SEs makes it desirable to be able to control this phenomenon, which requires the understanding of the elementary physical mechanism leading to their generation and emission. This paper reports on the dissection of such a tangled process operated by the help of spectroscopic tools of increasing finesse; measuring differential cross sections with an increasing degree of differentiation. These results demonstrate that single ionising scattering events, assisted by collective excitations, constitute the fundamental ingredient leading to SE-generation and -emission. To this end, the interaction of Low Energy Electrons (LEEs) with various Carbon allotropes has been investigated by means of Total Electron Yield (TEY) and (e,2e)-coincidence spectroscopy measurements. Carbon allotropes are chosen as targets since they are important in technological applications where both minimisation and maximisation of the SE-yield is a relevant issue. This is the first time that such complete set of benchmarks on the SE-yield from well characterised surfaces has been gathered, interpreted and is made available to the scientific community. This comprehensive investigation has led to the disentanglement of the elementary processes relevant for the understanding of the SE-generation probability, that fully take into account both energy and momentum conservation in the collision and the band structure of the solid as well as many-body effects.

1. Motivation

Bombardment of solid surfaces by a beam of electrons leads to promotion of solid state electrons to empty states, which can be emitted from the solid provided that they have sufficiently high kinetic energy to overcome the surface barrier. These so-called Secondary Electrons (SEs) play an important role in many scientific and technological applications. For example, SEs are essential for the visualisation of nanostructured materials in the Secondary Electron Microscope [1–3]. In scientific apparatus for charged particles spectroscopies, Secondary Electron Emission (SEE) is undesirable in electron optical elements, while, in the same instrument, it is sought for and exploited in the detection of the charged particles [4,5]. Low-Energy SEs (LE-SEs) can critically affect the operation of large research facilities, such as particle accelerators and charged particle storage rings, e.g. in the Large Hadron Collider (LHC) at CERN, since they can lead to electron cloud formation and consequently to a heat-load and pressure rise, through multipacting [6–9]. Mitigation of the electron cloud becomes particularly important when the high-luminosity mode will be taken into operation [10–12]. The surface charging of spacecraft materials induced by cosmic radiation represents one of the major issues for earth-orbiting space crafts limiting their performance and lifetime [13–16]. Detailed understanding concerning the mechanism of emission of Low Energy Electrons (LEEs) is also of relevance for the plasma-wall interaction in a fusion reactor, since SEs emitted from the surface of the vessel containing the plasma govern the plasma stability to an important degree [17]. The energy and charge balance of gaseous electronics such as plasma display panels [18,19] is a further example of relevance of SEE in technological devices. The above applications concern phenomena where the emission of LEEs into final states above the vacuum level are relevant. There is however, an important class of applications where the creation of secondary electrons in the form of *hot electrons* – these are

* Corresponding author at: ETHZ, Laboratorium für Festkörperphysik und Mikrostrukturen, Auguste-Piccard Hof 1, HPT C 2.2, CH-8093 Zürich, Switzerland.
E-mail address: abelliss@phys.ethz.ch (A. Bellissimo).

https://doi.org/10.1016/j.elspec.2019.07.004
Received 5 January 2019; Received in revised form 12 June 2019; Accepted 9 July 2019
Available online 21 August 2019
0368-2048/ © 2019 The Authors. Published by Elsevier B.V. This is an open access article under the CC BY license (http://creativecommons.org/licenses/BY/4.0/).

electrons below the vacuum level – is causing either desired or undesired effects. In the case of biological tissue, LEEs cause damage in the form of bond breaking of DNA which may lead to tumor formation, but at the same time the application of LEEs for therapeutic purposes is also being investigated [20]. In Electron Beam Lithography the attainable lateral resolution can be compromised due to the so-called proximity effect – the random migration of LE-SEs and hot electrons within the photo-resist [21,22]. Similar problems are encountered in the patterning technique of Focused Electron Beam Induced Deposition [23]. LE-SEs, as well as hot-electrons, can constitute a big nuisance that needs to be eliminated, affecting the functioning of semiconductor devices (e.g. transistors) [24] and insulators [25,26] in microelectronics, but at the same time their existence is exploited in photovoltaic devices [27].

While the phenomenon of secondary electron emission has been extensively studied by many authors (see e.g. the reviews presented in Refs. [1,28–31]), presently, more than a century after the discovery of the electron, there are still essential fundamental, yet unresolved, questions concerning their creation-ejection mechanisms. The applications mentioned above make it clear that while SEE is exploited in some cases, it can be highly undesirable in others. Therefore, generally speaking, it is advantageous to be able to control this phenomenon to some extent. This requires understanding the fundamental physical mechanism leading to the emission of SEs from solid surfaces. Quantitative investigation of the emission mechanisms is complicated by the fact that the energy deposition of the primary beam proceeds via plural (and multiple) inelastic scattering processes, in each of which energy and momentum are transferred to the solid state electrons. These can in turn experience (plural and subsequent) inelastic processes, which may ultimately lead to the formation of a *cascade* of LEEs. As a consequence of the formation of the LE-cascade inside the solid, the details of fundamental interaction processes are smeared out and the emitted energy distribution becomes essentially featureless, i.e. SE-spectral features can be buried underneath this broad distribution. This is generally true, especially in case of polycrystalline and amorphous materials. The lack of long-range order implies that the ejection of SEs must be regarded by averaging over all symmetry directions available in the target. Whereas in case of single crystals, or in materials such as Highly Oriented Pyrolytic Graphite (HOPG) – characterised by a high degree of in-plane order extended over a 3D-crystalline structure – exhibiting a band structure with a complexity beyond those of simple metals, the SE-spectrum can display a whole manifold of distinct spectral features (see e.g. Fig. 2 below). These SE-spectral features are linked to ejected electrons having a well-defined momentum, which is characteristic for the unoccupied electron band through which they escape to vacuum. Shape and intensity of these characteristic peaks in the SEE-spectrum of crystals are dictated by the electronic structure of the conduction band. It is in fact well known, that by means of (angle-resolved) SEE-spectroscopy, it is possible to perform a band mapping of the unoccupied states in a crystal (e.g. as discussed in Refs. [32,33], to name a few).

In this work, the energy labelled as E_0 defines the primary energy of the electron beam, used in a simulation or experiment. E_0 is given with respect to the vacuum level of the target.

Fig. 1 shows the results of Monte Carlo (MC) simulations yielding the energy distribution of all electrons (scattered and emitted) from a polycrystalline Gold surface [34]. The energy of all these electrons taking off from the sample is given w.r.t. the vacuum level. These model calculations are purely classical, therefore it is essentially possible to distinguish between a *scattered* and an *ejected* electron, for arbitrary combinations of their kinetic energies. Spectral features, characteristic for inelastic loss processes can be distinguished near the peak of elastically backscattered electrons at $E_0 = 1000$ eV, whereas the SE-peak at energies ($E - E_{vac}$) below ~50 eV is substantially bland.

The model calculations of Fig. 1 clearly show that secondary electrons (red dashed-dotted curve in Fig. 1) with considerable kinetic energies, of the order of the elastic peak energy, may be emitted from the surface, although the majority is released with energies below

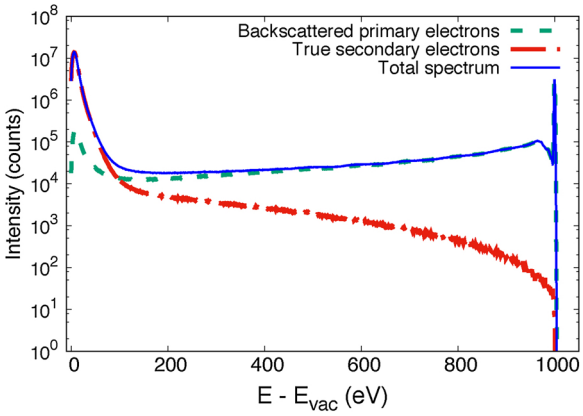

Fig. 1. Classical Monte Carlo simulation of an electron spectrum from a Gold surface, for a primary electron energy E_0 of 1000 eV (given with respect to vacuum level). The total energy distribution (blue solid curve) is made up of backscattered primary electrons (green dashed curve) and secondary electrons (red dashed-dotted curve).

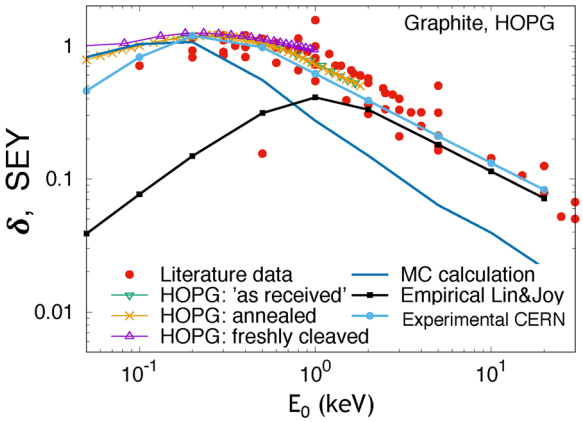

Fig. 2. Comparison of experimental SEY data with the results of calculations based on the Monte Carlo simulation and the semi-empirical formula. MC calculations (thin blue line) were made for amorphous Carbon neglecting the anisotropy of the dielectric function.

~50 eV. For such low energies, the contribution of backscattered primaries (green dashed curve in Fig. 1) to the total spectrum is more than an order of magnitude smaller than the contribution of secondaries, which is the reason why, *by convention* electrons with vacuum energies below ~50 eV are designated as (*true*) secondary electrons. The physical reason for the peak at energies below ~50 eV is the fact that the typical energy of the solid state electrons is of the order of 1 Hartree (27.22 eV) [35], giving rise to a mean energy loss in an inelastic collision of the same order of magnitude, for arbitrary incident energies.

The number of SEs emitted per incident electron is defined as the Secondary Electron Yield (SEY). In view of the fact that it is experimentally impossible to distinguish between true secondary electrons and backscattered primaries, it is important to realise that the fraction of backscattered primaries in the spectral region below ~50 eV may be significant when comparing experimental and theoretical data for the SEY, in particular at low incident energies ($E_0 \leq 100$ eV). The quantity accessible to experiment is, in fact, the Total Electron Yield (TEY), σ, rather than the SEY, δ, which together with the reflection coefficient η makes up the total current of the spectrum (see Fig. 1):

$$\sigma = \delta + \eta \tag{1}$$

Due to the formation of the cascade leading to an energy spectrum of secondary electrons, SE-emission is still far from being quantitatively understood. While the different excitation channels can be easily

discriminated with Electron Energy-Loss Spectroscopy (EELS), the mechanism by which the deposited energy (and its associated momentum) is distributed over the degrees of freedom of the solid is not easily resolvable by experiment. It is obvious that this requires the detection of *correlated* electron pairs, where one electron carries the signature of the involved energy loss process, while the other electron of the pair provides information on how the energy and momentum transferred by the incoming electron is dissipated away by the solid. Such an experiment, known as (e,2e)-coincidence spectroscopy – a *"one electron in, two electrons out"*-technique – enables to completely determine the kinematics of an ionisation process. (e,2e)-coincidence spectroscopy is therefore ideally suited to study electron correlation effects and allows to directly link the Energy Loss Spectrum (ELS) to the SE-spectrum by collecting time-correlated electron pairs, i.e. two electrons that have participated in the same collision event. In other words, it is possible in this way to investigate individual processes in which both the initial and the final state are fixed and wherein the transferred momentum and energy fully describe the occurring electronic transition. This should be compared to conventional (non-coincident or singles) measurements of the SE-spectrum where only the final state is defined or to singles EELS where many combinations of initial and final states contribute to the intensity measured at a given energy.

The pioneering work by Amaldi et al. [36] followed by the work of Camilloni et al. [37] already demonstrated that the (e,2e) technique is a powerful tool for the detailed investigation of the ionisation mechanisms. Over the past 50 years the interest for this technique, in particular as applied to solid surfaces, has been growing and has been further developed by several groups [38–48].

In the present paper, different aspects of the interaction of LEEs with various Carbon allotropes are investigated by means of TEY and (e,2e)-coincidence spectroscopy. The ultimate aim of the present work is to define the ingredients for a quantitative model describing SEE for a material with an electronic structure more complex than that of simple metals, which may form the basis of a more general model for the phenomenon. To this end, a better understanding of individual elementary processes being at the core of SEE is needed.

Carbon allotropes are chosen since they are known to have a low SEY and are therefore important in technological applications where minimisation of the SEY of surfaces is a relevant issue. Furthermore, graphite and C-based materials constitute a prototype for layered electron gas (LEG) structures [49,50].

2. Survey of the existing models for SEE

There are three main steps to describe the secondary electron emission process: (1) transport of a primary electron in a solid, (2) generation of a secondary electron, and (3) transport and escape over the surface potential barrier of the produced SE. Electron transport for both primary and secondary electrons proceeds through elastic and inelastic scattering. For many applications, in which materials with short-range order are employed, the transport of electrons can be conveniently described by means of non-coherent scattering of particles. When crystalline samples are involved, it is necessary to take into account the wave nature of electrons.

Non-coherent electron transport can be dealt by solving the Boltzmann-type kinetic equation, whereas for coherent scattering the Schrödinger equation must be solved.

In this connection, it should be mentioned that theories for electron transport in crystalline media exist for different surface characterisation techniques [51–55] and are based on a rigorous treatment of the Schrödinger equation. However, the description is usually restricted to (elastic) peak intensities, while consistent treatment of energy loss processes is usually lacking (except for Ref. [55]). In these theoretical approaches, the creation, propagation and emission of secondary electrons, which is the main subject of the present paper, does not seem to have been even attempted presently. Loss of coherence, e.g. due to imperfections in a crystal, may formally be understood by the vanishing of the off-diagonal terms in the density matrix [56–59], which describe quantum-mechanical interference. The problem of describing the electron transport in solids then reduces to solving a Boltzmann-type kinetic equation.

The non-coherent electron transport in a solid is assumed to comprise elastic and inelastic scattering. Elastic scattering describes the interaction of an electron with the ionic subsystem of the solid. Such an interaction between the electron and a nucleus involves a deflection of the electron by the (screened) Coulomb field of the nucleus, accompanied by a small recoil energy loss. Due to the large mass difference between electron and nucleus this energy loss is negligible compared to any energy loss experienced in inelastic collisions. Inelastic scattering involves the interaction of an electron with the solid state electrons, accompanied by a small momentum transfer and a large energy loss compared to the recoil energy loss in elastic collisions. The transport mean free path (TRMFP) – a measure for the momentum transfer along the initial direction – during inelastic scattering is usually one order of magnitude larger than the transport mean free path for elastic scattering [60]. This fact allows to neglect the deflections during inelastic collisions.

When the wave nature of an electron can be neglected, i.e. the electron wavelength is much smaller than the inter-atomic distance, the binary encounter approximation becomes applicable. This approach assumes that the volume occupied by an atom significantly exceeds the volume in which the electron interaction takes place [60]. This condition is generally satisfied for high/medium-energy electrons, whereas for Low Energy Electrons [61] this is no longer valid since the electron wavelengths become comparable or even larger than the inter-atomic distance. For example, for an electron with energy 100 eV the correspondent wavelength is of the order of 1 Å, which is already comparable with inter-atomic distances. For an electron just above the vacuum level, e.g. of 1 eV, the electron wavelength exceeds the inter-atomic distance by a factor of ca. 4 or 6 (depending on the lattice parameter), since it becomes about 12 Å. However, inside the solid the maximum wavelength for an electron detected in vacuum is dictated by the height of the inner potential (about 20 eV), i.e. it is about 3 Å.

Finding a solution to the Boltzmann transport equation is a complicated task. Therefore, one has to resort to numerical solution techniques or to employ approximate approaches [62,63]. One of the most popular ways is to make use of a Monte Carlo (MC) simulation. Nowadays, the MC technique is described in detail by many authors in the literature, e.g. [60,64,65]. Many of them employ the continuous slowing down approximation (CSDA) to describe multiple electron scattering assuming that energy fluctuations after a given path length are weak [60]. Note, that this does not account for the elastic peak or the quasi-elastic and the accompanying energy loss features observed in an experiment. Nevertheless, this simple approach has been successfully applied to describe electron induced X-ray production in solids [66]. However, since the details of individual scattering processes are not taken into account, a direct simulation approach in which energy fluctuations are considered must be used in the case of the simulation of secondary electron emission processes. In Ref. [34] in this issue the application of this direct MC algorithm for secondary electron generation and emission is explained in some detail. This type of the MC model is based on the generation of electron trajectories assuming linear electron paths interrupted by scattering events. The description of elastic scattering requires data for the elastic mean free path, the total and differential elastic cross section (DECS). Different codes are available for the calculation of the DECS. One of the most reliable and frequently used approaches is the ELSEPA code [67]. It is presently not completely clear what the lower limits of validity of the elastic cross sections obtained in this way are. For the energy range important for the transport of SEs it is expected that the elastic cross sections become unreliable due to absorption and correlation effects (see Ref. [67] for an extensive review). To describe inelastic scattering, data for the inelastic

mean free path (IMFP), the total inelastic cross section and the differential inverse inelastic mean free path (DIIMFP) are required. The IMFP is defined as the average path length an electron travels in between two successive inelastic collisions measured along the electron trajectory. The DIIMFP describes the distribution of single energy losses during the inelastic scattering process. The DIIMFP and IMFP can be obtained on the basis of linear response theory using optical constants [68–71]. However, in the LE-regime there is a huge spread for IMFP values reported in literature [34], which introduces limitations for the reliability of the MC simulation below 100 eV.

The inelastic interaction of an impinging electron with valence band electrons leads to an energy loss ΔE with a subsequent generation of a SE. Usually it is assumed that SEs are mainly ejected from the Fermi level [65]. There was an attempt made by the authors of Ref. [64] to consider electron emission from anywhere within the valence band. This causes a reduction of the SEY since a larger fraction of SEs has a smaller energy and cannot escape over the surface barrier. Furthermore, an additional issue related to energy loss events is whether each such a collision generates a single secondary electron or a swarm of secondaries, instead. Earlier work [72] as well as Ref. [73] suggest that the single electron generation process is dominant. However, the possibility of creating multiple electrons in a single collision cannot be ruled out.

Penetration through the surface potential barrier (along the surface normal) is determined by two parameters, the sample workfunction Φ_s and the (mean) inner potential U_{in}. The value of the inner potential U_{in} is usually taken to be the sum of the Fermi energy E_{Fermi} and Φ_s, which is generally known with reasonable accuracy [74]. However, there is a spread between U_{in} values in the literature [75]. Furthermore, for the case of off-normal trespassing of the surface refraction between media of different refractive index (in the complete analogy to Snell's law for photons) must be taken into account (for more details see Ref. [34] in the same issue).

Taking into account all the assumptions and limitations mentioned above, the MC approach becomes questionable, in particular for the investigation of LEEs. Nevertheless, MC simulations seem to work quite reasonably for many applications such as calculations of ELS, inelastic back-scattering coefficients and SEYs for energies ranging between 50 eV and MeV [34] and is frequently employed by many authors.

The commonly employed semi-empirical formula to predict the SEY (or δ) as a function of the incident energy (E_0) is given by Lin and Joy in [76]. They compiled and examined a huge database of experimentally measured SEY curves acquired over a period of 80 years by many authors, covering 51 elements and 42 compounds and exhibiting a rather large spread among SEY curves for a same material. Such a divergence between SEY data can be brought in connection to different surface preparation and measurement methods. In addition, it shall be mentioned, that in the case of so-called “technical surfaces”, e.g. those of an accelerator beam pipe, which are generally covered by an oxide layer and other contaminants, this formula is not applicable. After scrutinising this data base the authors derived a “*universal law*” by fitting MC calculations employing the CSDA in the form of Eq. (2) thus to describe the experimental data:

$$\frac{\delta}{\delta_{\max}} = 1.28\left(\frac{E_0}{E_0^{\max}}\right)^{-0.67} \times \left(1 - \exp\left(-1.614\left(\frac{E_0}{E_0^{\max}}\right)^{1.67}\right)\right) \tag{2}$$

where the yield is parametrised in terms of the maximum SE yield δ_{max} and the corresponding primary energy $E_0^{\max}$. The scope of this formula was intended to be used as a tool to examine sets of experimental results, to identify possible sources of error in the data, and to generate an optimised SE-yield profile for the element of interest. Fig. 2 shows the comparison of the results of calculations based on this semi-empirical formula, given in Eq. (2), with experimental SEY data. Red data points correspond to the collection of SEY values from the literature [76]. The curves labelled ‘Empirical Lin&Joy’ (black dotted) and ‘Experimental CERN’ (light blue line with diamonds) were calculated according to Eq. (2). In the first case, the δ_{max} and $E_0^{\max}$ values used for the computation were taken from [76], whereas in the second case these values were obtained from SEY measurements performed at CERN (Fig. 8).

The SEY curves in Fig. 2 are plotted on a logarithmic scale to highlight the divergence between the calculation and the experimental data seen at both lower energies ($\lesssim$200 eV) and at higher energies ($\geq$1000 eV). While the ‘Experimental CERN’ curve yields an overall agreement with other experiments (red points) the ‘MC calculation’ and the ‘Empirical Lin&Joy’ fail at low and high energies, respectively. These discrepancies suggest that the commonly employed universal law does not cover all the details of the mechanisms playing a role in secondary electron emission. It should be kept in mind, that for practical applications a difference between a δ_{max} of 1 and 1.3 (not appreciable on this logarithmic scale) can be indeed crucial and need to be considered.

There is also an empirical approach to predict the SE-Emission Spectrum (SEES) which was introduced by Chung and Everhart [77]:

$$\frac{\mathrm{dj}(E)}{\mathrm{dE}} = \kappa \frac{E}{(E + \Phi_s)^4} \tag{3}$$

Here, $dj(E)/dE$ is the differential energy distribution of SEs at the emitted energy, E, measured with respect to the vacuum level, and κ is a normalisation constant. Fig. 3 shows the comparison of measured SEES of HOPG (black line) and randomly oriented glassy Carbon (gl-C) (red dashed line) with Eq. (3). For these materials the prediction of the SE-spectrum using this formula does not provide a reasonable description of the experimental data. Despite the fact that such semi-empirical formulae are very convenient, Figs. 2 and 3 demonstrate that they can be successfully applied only to obtain qualitative estimates, thus predicting only the functional dependence of SEE, but not its magnitude, a further indicator of deficient quantitative understanding. As seen from Fig. 3 there is a big difference between spectra for HOPG and gl-C due to the different (crystalline) order of these materials. Therefore the prediction of any physical quantities describing the SEE, such as the SEY, for any Carbon allotrope still requires the much more detailed investigation of the mechanisms of the secondary electron generation, the transport of LEEs in crystalline and non-crystalline solids, and the corresponding band structure.

3. Experimental

3.1. Experimental: sample preparation

The set of Carbon allotropes chosen for our investigations comprehends two Highly Oriented Pyrolytic Graphite (HOPG) surfaces, a

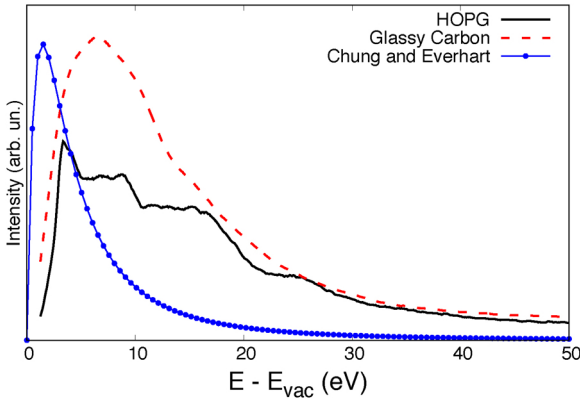

Fig. 3. Comparison of experimental SEES from HOPG (black solid) and gl-C (red dashed) measured with an electron beam energy of E_0 = 173 eV with the result of the empirical formula given in Eq. (3), for the prediction of a secondary electron spectrum (blue dotted).

glassy Carbon (gl-C) and an amorphous Carbon coating (a-C). These samples exhibit all a similar microscopic electronic structure, but different long-range orders, hence the Density-of-States (DoS) can vary among different allotropes.

HOPG is a semi-metal characterised by a high degree of in-plane order extended over a 3D-crystalline structure, consisting of identical stacked graphitic planes with outstanding regularity and smoothness at nanoscale. The quality – associated to the degree of crystalline order along the $\hat{c}$-axis – of these specimens is generally defined by the so-called mosaic spread describing the angular spread in-between graphitic layers. The graphitic planes are, in turn, composed of a mixture of tiles oriented in all symmetry directions in-between the two main in-plane symmetry directions of graphite – ΓK and ΓM.

In the laboratory of the Università di Roma Tre (RM3) a HOPG specimen of the ZYA quality, with a nominal mosaic spread of 0.4° ± 0.1°, was employed. The same sample was also used for the TEY-measurements performed at CERN. In the laboratory of the Technical University in Vienna (TUV) measurements were performed on a HOPG surface of ZYB quality with a nominal mosaic spread of 0.8° ± 0.2°. In all laboratories, the HOPG-surface was prepared by means of mechanical exfoliation followed by a cycle of annealing (at a temperature of 480 °C at RM3 and up to 500 °C at TUV). Exfoliation of the sample exposes a fresh uncontaminated surface. Annealing in a Ultra-High Vacuum (UHV) environment is necessary to get rid of adsorbed and intercalated water. Residual gas analysis during the annealing showed that the water was successfully removed.

The cleanliness of the surfaces was verified by means of X-ray Photoelectron Spectroscopy (XPS) or of Auger Electron Spectroscopy (AES) and the crystalline order was monitored by means of Low-Energy Electron Diffraction (LEED) scans (see left panel in Fig. 4). In a LEED scan, the sample surface is rotated with respect to both source and analyser, thus leading to a variation of the scattering geometry. In such an angular scan, the change of incidence and emission angles (θ_i; θ_o) induces a variation of the parallel component of the exchanged momentum ($\Delta\vec{K}_{\parallel}$) as indicated on the ordinate axis of the left panel in Fig. 4. Fulfilment of the Bragg condition is given when this momentum transfer component equals the in-plane reciprocal lattice vector in a given symmetry direction, either $\vec{G}_{\Gamma K}$ or $\vec{G}_{\Gamma M}$, or also when it equals combinations of these G-vectors.

The rocking curve of the elastically reflected electrons shown in the left panel of Fig. 4 demonstrates that for the chosen kinematics, both symmetry directions contribute to the diffusion of scattered electrons confirming the existence of domains with different azimuthal orientation. A first order diffraction peak along the ΓK-direction is indicated by the blue arrow. For this scattering geometry the parallel component of the exchanged momentum projected onto the surface, $\Delta K_{\parallel}$, yields the reciprocal lattice vector $|\vec{G}_{\Gamma K}| = 5.10$ Å^{-1} for the ΓK-symmetry direction. Diffraction peaks along ΓM-direction are measured up to the second order Bragg-diffraction (with the first order diffraction peak indicated by the red arrow with $\Delta K_{\parallel} = |\vec{G}_{\Gamma M}| = 2.94$ Å^{-1}). The two outermost peaks (on the left and right-hand side, indicated by the purple arrow) correspond to a superposition of the two main in-plane reciprocal lattice vectors, yielding a $\Delta\vec{K}_{\parallel}$ equal to the sum of $|\vec{G}_{\Gamma K} + \vec{G}_{\Gamma M}|$. The right panel of the same figure illustrates the two dimensional Brillouin zone (BZ) of graphite highlighting the two main in-plane symmetry directions. Both lattice vectors of the two main in-plane symmetry directions determined by this analysis agree with known data [78–81].

Glassy Carbon (gl-C) unifies typical characteristics of ceramic, or vitreous materials, with those of graphite. The electronic structure of gl-C, just like in the case of HOPG, is entirely composed of sp^2-hybrids giving rise to the typical 2D-honeycomb lattice. In case of gl-C the graphitic planes form interwoven ribbons with random orientation, therefore comprising all possible geometrical arrangements for a sheet. This sample was used only at TUV to perform (e,2e)-coincidence measurements and Reflection Electron Energy Loss (REELS) measurements. Gl-C was cleaned with ethanol and blown dry with air. In order to remove the leftover contaminants, it was sputtered with 4 keV Argon ions for half an hour and subsequently annealed at 500 °C. The removal of contaminants was confirmed by XPS and by the appearance of the π-plasmon in the REELS spectrum, which was not distinguishable before sputtering.

An amorphous Carbon coating (a-C) (lacking any crystalline order) typically used to reduce the secondary electron yield inside the beam-pipes of the vacuum system in the Super Proton Syncrotron (SPS) of the LHC [82] was prepared for the TEY-investigations done at CERN. The a-C coating was sputtered with 3 keV Argon ions and the cleanliness of the surface was monitored by means of XPS during sputtering. The annealing cycle was performed for ca. two hours at a maximal temperature of 250 °C. A lower annealing temperature was chosen in this case to avoid detachment of the coating from the substrate. However, this choice was found to be conservative, since similar a-C coatings produced at CERN are routinely annealed up to 400 °C.

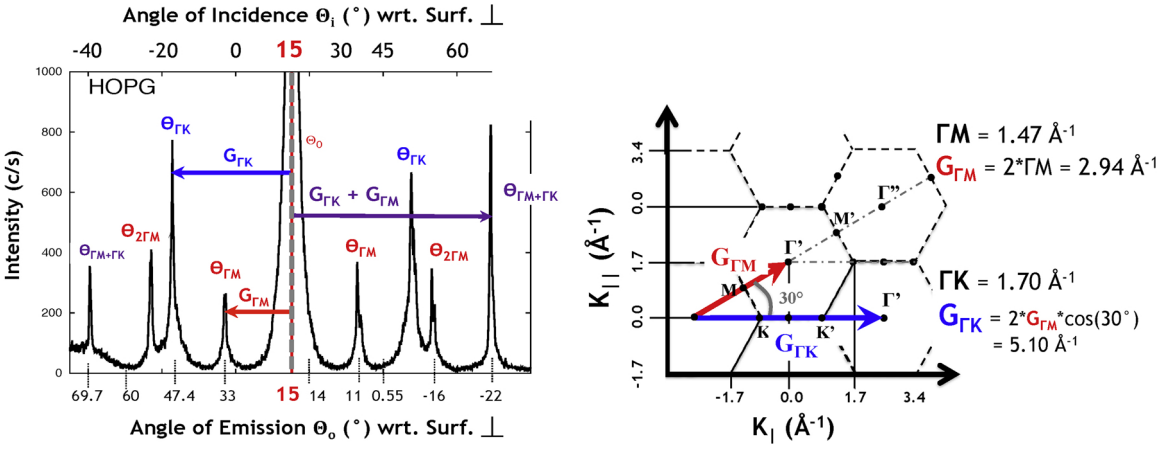

Fig. 4. *Left panel:* Diffraction pattern from HOPG of the elastically scattered electrons ($E_0 = 91.73$ eV), where specular reflection conditions are obtained for $\theta_i = \theta_o = 15°$. The specular peak has an angular width of 0.5° at FWHM. Diffraction peaks given along the two main symmetry directions of ΓK and ΓM as well as intermediate ones are indicated by arrows. *Right panel:* In-plane Brillouin zone of graphite with reciprocal lattice vectors highlighted in red ($\vec{G}_{\Gamma M}$) and blue ($\vec{G}_{\Gamma K}$).

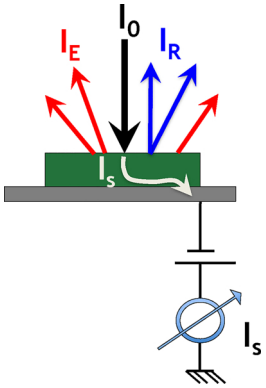

Fig. 5. Experimental set-up used at CERN to perform TEY-measurements based on a retarding potential measurement layout. Sample bombardment is shown under normal incidence indicated by the black arrow associated to I_0. The scheme illustrates the case when a negative bias ($V_{bias} < 0$ V) is applied on the target. The current drained by the sample, I_s, is linked to absorbed electrons with an energy greater than the applied bias, thus excluding current contributions of the ejected electrons (I_E) with energies lower than $e{\cdot}V_{bias}$. For each primary energy, E_0, the TEY-value is obtained according to Eq. (5).

3.2. Experimental: measuring the TEY

The Total Electron Yield σ, of a material is in general measured for perpendicular incidence ($\theta_i = 0°$) of electrons as a function of the impact energy ranging up to several keV. The experimental method relies on Total Current Spectroscopy [83], schematically shown in Fig. 5, where an electron beam impinges on a sample and σ is investigated by monitoring the target current. In such a measurement the target – with a given workfunction Φ_s – is set to a (fix) potential V_{bias} (of arbitrary value) and the electron gun irradiates the sample with a source energy, E_0, defined by $e{\cdot}U_{gun} + \Phi_{fil}$, where e is the elementary (positive) charge, U_{gun} is the potential set at the electron gun given with respect to the common Fermi level of the apparatus and Φ_{fil} is the workfunction of the filament of the electron source. Application of a V_{bias} onto the sample does not change the energy of the electron beam leaving the gun, but it does affect the effective impact energy of the electron beam reaching the sample surface. This effective (*landing*) energy of the electron impinging on the biased sample is defined w.r.t. the vacuum level as follows:

$$\begin{aligned}(E - E_{vac}) &= e{\cdot}(U_{gun} - V_{bias}) + \Phi_{fil} - \Phi_s \\ &= E_0 - (e{\cdot}V_{bias} + \Phi_s)\end{aligned} \quad (4)$$

The right-hand side of Eq. (4) contains the energy of the electron as it is emitted from the gun (E_0) and the potential of the sample surface, both with respect to the common Fermi level ($\Phi_s + e{\cdot}V_{bias}$) of the apparatus. Their difference therefore defines the energy of the electrons landing on the sample surface.

To assure the performance of TEY measurements in the LE-range it is necessary to compensate the Earth's magnetic field in the scattering region. A μ-metal shielding of the vacuum vessel is used to minimise the influence of the magnetic field. Especially when operating with very Low Energy Electrons, calibration of the electron energy scale represents an essential step prior to the actual measurement (see further in text). Furthermore, from Eq. (4) it can be understood that once the electron energy scale has been calibrated, the U_{fil} for which ($E - E_{vac}$) becomes zero allows to determine, through Eq. (4), the sample work function.

Fig. 5 gives a schematic representation of the instrumentation used in this work for the series of TEY-measurements presented in Section (4). The TEY – already defined in terms of σ, η and δ in Eq. (1) – as a function of electron energy, is experimentally obtained by

$$\sigma = \frac{I_0 - I_s}{I_0} \quad (5)$$

where I_0 represents the total impinging (or primary) current and I_s is the sample current, both measured over the whole effective landing energy range of interest. In either case, the current is measured as the current drained by the bombarded target via a pico-amperometre (as sketched in Fig. 5). The measurement of σ is performed in two steps. In the first step, we measure the total incident current I_0, as a function of an increasing E_0. A constant positive V_{bias}, e.g. of +45 V, is applied to the target to ensure that all electrons are detected. The electron source energy E_0 is scanned in small steps from e.g. 43 eV up to the maximum energy of interest. In this case all electrons are collected by the sample and recorded by the pico-amperometre – measuring the sample current. In addition, I_0 is routinely compared to the primary current measured using a Faraday cup, to assure consistency. In the second step, the polarity of V_{bias} is inverted (becoming −45 V) to ensure that all secondary electrons are excluded from the current measurement. V_{bias} is again fixed for the whole energy scan. For $V_{bias} < 0$ V (the case represented in Fig. 5) the measured sample current, I_s, is equal to the current of absorbed electrons excluding contributions given by the ejected electrons, I_E, generated in the course of the electron beam-specimen interaction. Note that this approach allows one to measure the yield curve down to 0 eV-landing energy in a stable reproducible manner. Reflected electrons (with I_R) do not give any net contribution to the I_s irrespective of the fact whether they can reach the surface or not for a given sample bias.

To assure the accuracy of TEY measurements in the LE-range it is necessary to (regularly) perform a calibration of the absolute energy scale, since emission from the electron gun filament may vary with time and pressure conditions, e.g. induced by changes in Φ_{fil} after prolonged emission. The calibration of the electron energy scale is provided by measuring the low-energy (LE) TEY curve from a clean polycrystalline Gold surface, of which the workfunction, $\Phi_{Au} = 5.2$ eV, is known [84,85] and defines the energy scale in our following experiments.

Fig. 6 entails two LE-TEY curves acquired on polycrystalline Gold (black) and Copper (orange). Irrespective of the target and for negative values of the electron landing energies ($E - E_{vac}$) LE-TEY curves are expected to exhibit a σ of 1, as indeed seen in Fig. 6. In this case, all impinging electrons are reflected by the sample surface, which acts as a barrier. This constant yield of 1 is followed by a sudden drop. This drop of σ – visible as a descending slope in Fig. 6 – is expected to happen exactly at ($E - E_{vac}$) = 0 eV, which depends on the material, i.e. on Φ_s, which can be determined through the relation given in Eq. (4). It is linked to a decrease in reflectivity, η, and, consequently, to an increased penetration of the incoming electrons into the target.

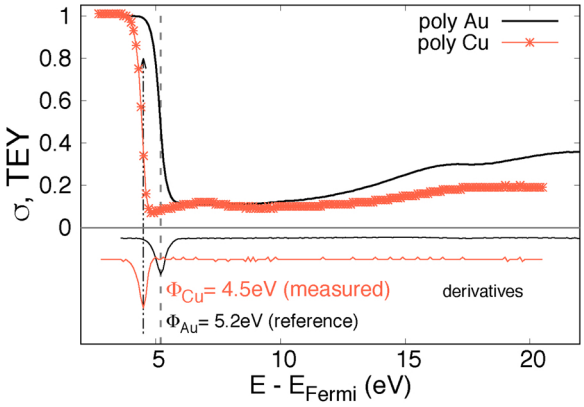

Fig. 6. LE-TEY curves from clean polycrystalline Au and Cu surfaces. First derivatives of σ (shown at the bottom for "$\sigma < 0$″) exhibit minima in correspondence of the inflection points yielding Φ_s values. Electron energies are given w.r.t. the common Fermi level.

Under the assumption of a sharp surface potential barrier, at the workfunction, Φ_s, one should expect a sharp step, but the energy spread of the electron beam turns the step-function into a descending slope of a given determined by the energy spread of the beam (a Gaussian with a FWHM of ~0.5 eV). The workfunction of a material can be conveniently obtained by making the first derivative of the LE-TEY curve, where the inflection point is found at the minimum.

For the polycrystalline Au surface (shown as black continuous curve in Fig. 6), the workfunction amounts to 5.2 eV, fixing the absolute energy reference of the electron energy scale. After this calibration of the energy scale, the (orange) curve with data points shown in Fig. 6 is the LE-TEY measurement performed on a clean polycrystalline Copper surface, for which the inflection point is seen around 4.5 ± 0.2 eV. Within the error bars, this value agrees with an additional in situ Kelvin probe measurement, corresponding to the expected value of Φ_{Cu} for polycrystalline Cu [84]. To highlight the fact that by measuring the LE-TEY curve of a material it is also possible to determine its workfunction, σ in Fig. 6 are displayed as a function of the electron energy defined w.r.t. the common Fermi level. By further increasing the source energy, effectively increasing the electron landing energy, a monotonous increase of σ is observed. For higher energies the structure of the LE-TEY for both samples exhibits some faint features. In Section (4) it will be demonstrated, that for the proper interpretation of these and similar structures, it is necessary to take into account the (unoccupied) electronic structure of the target and, as already discussed by authors of Refs. [86–88], to consider the allowed electron transitions, which again relate to the final-state band structure. In case of crystalline targets exhibiting well-defined high-symmetry directions, this increase of σ is often not at all smooth and strongly reflects band gaps found in the electronic structure above vacuum level. As pointed out by Strocov, Barrett et al. in their works [89–91], in order to describe the emission properties in ordered materials, knowledge on the final-state band structure is mandatory. An example for such a modulated (non-smooth) σ curve – measured on HOPG – is shown in Fig. 10 and is discussed in detail in Section (4).

In general, the higher the electron incident energy, the more the total yield is dominated by the contribution of the inelastically scattered primaries, as well as the directly emitted electrons (SEs) from the solid. An experiment conducted in another apparatus (described elsewhere [92,93]) and involving primary electron energies up to 1800 eV, allowed to separate the elastically reflected and inelastically backscattered electrons (η) from the generated SEs (δ). According to these measured partial yields (not shown), we could determine that for primary energies ranging from ca. 80 eV up to 500 eV, the TEY is made up to ca. 90% by SEs only. This justifies that in the higher energy range (≥80 eV) one generally refers to the TEY as *secondary* electron yield (SEY).

3.3. Experimental: measuring the (e,2e)-coincidence spectrum

The (e,2e)-coincidence measurements were performed in the SE2ELCS (Secondary Electron-Electron Energy Loss Coincidence Spectroscopy) spectrometer at the Vienna University of Technology and in the (e,2e)-spectrometer in the LASEC (LAboratorio di Spettroscopie Elettroniche e Correlazioni) at Università degli Studi Roma Tre. Due to their different geometrical configurations (see Fig. 7 for details), each instrument is capable to study the same scattering process, the resolved in-parallel component of the exchanged momentum ($\Delta\vec{K}_{\parallel} = \vec{k}_0 - \vec{k}_s$) under different kinematics, i.e. for a same energy loss ($\Delta E = E_0 - E_s$) and different $\Delta\vec{K}_{\parallel}$.

In an (e,2e)-coincidence experiment the primary electron (defined by E_0 and $\vec{k}_0$) impinges onto the target and transfers part (or all) of its energy and momentum to the electronic sub-system during an inelastic scattering event. This inelastically scattered electron is then detected simultaneously within a time resolution of few *ns*, i.e. coincident in time, with an ejected SE and their energy ($E_{s,e}$) and momenta ($\vec{k}_{s,e}$) are measured. By means of energy and momentum balance the complete kinematics of the process are reconstructed. The subscripts *"0,s,e"* stand for primary, (inelastically) scattered and ejected electrons, respectively.

Hence, in such an (e,2e)-measurement, the SE-yield is measured simultaneously with the energy loss spectrum (ELS), since the acquisition of *time-correlated* electron pairs enables to directly link a specific energy loss to an ejected electron of a given kinetic energy and vice versa. Probability of emission of the scattered-ejected electron pair is measured resolved in energy and momentum of the two individual electrons that are collected within the accepted solid angles $\Omega_s(\theta_s, \varphi_s)$ and $\Omega_e(\theta_e, \varphi_e)$ of the two analysers, each one of which is tuned on a different energy. By selecting the kinematics of the scattering process and by choosing both the energy and momentum transfers (ΔE and $\Delta\vec{K}$) occurring during the collision, the measured probability-flux – also (e,2e)-coincidence yield – corresponds to a triple-differential cross-section (TDCS). The measured TDCS is interpreted as a differential SE-yield, which is specific to a given energy loss ΔE undergone by the incident electron – differential in both energy and momentum. The resulting TDCS can be represented as a function of the energy loss undergone by the primary electron with respect to the ejected electron energy, E_e. Alternatively, it can be expressed as a function of the binding energy, ε_{bin}, and of the momentum of the bound electron prior to its emission, $\vec{q}$.

In SE2ELCS (illustrated on the left panel of Fig. 7) the sample is irradiated with a continuous beam of electrons, at currents below a picoampere. Back reflected electrons are detected with a hemispherical analyser (HMA), which is positioned in specular reflection with the electron gun at 60° with respect to the surface normal. The second detector is a Time-Of-Flight (TOF) analyser [94,95], which due to its' enhanced energy resolution at low energies and wide accepted solid angle (of the order of ± 10°) is used to collect the SEs emitted by inelastic collisions of the primary electron. During the measurement, the TOF analyser records event flight times, while the energy observed by the HMA is scanned from the incident energy down to several eV. The energy resolution at the HMA is 2.5% of the pass energy, whereas in the time-of-flight analyser the energy resolution depends on the kinetic energy of the detected electrons. A correlated electron pair – composed of a "fast" (inelastically scattered) electron and of a "slow" (ejected) electron – is assumed to be created within a few femtoseconds, this allows one to determine the flight time of the slower electron using the fast one as a "start" signal. The measurements are done in UHV, maintaining the pressure of $2 \cdot 10^{-10}$ mbar over the whole measurement duration (typically several weeks).

In SE2ELCS the sample-rotation is limited to a small range (of ca. ± 20°), not always allowing to reach higher order diffraction peaks. Therefore all (e,2e)-measurements are performed tuned on the zero-order Bragg peak. The best suited Bragg diffraction conditions (i.e. yielding the highest intensity) are found by performing energy scans at a fixed scattering geometry (commonly known as "*I-V-curves*"). In case of an I-V-curve, the sample position is kept constant (in specular reflection with $\theta_i = \theta_o$) while the energy of the primary electron beam is scanned from ca. 20 eV up to 500 eV, thus yielding an I-V-profile. Fulfilment of the third Bragg condition, i.e. in the perpendicular direction, ($\Delta\vec{K}_{\perp} = \vec{G}_{\Gamma A}$) leads to strong intensity variations in the reflected LEED peaks as a function of primary energy, E_0. At a vacuum-surface interface only the parallel component of the electron momentum, $\vec{k}_{l,\parallel}$ (with $l = 0, s, e$), is conserved, whereas in the bulk of the solid its energy and herewith the perpendicular component of its momentum ($k_{l,\perp,in}$) is changed upon transmission through the surface, under the influence of the so-called (crystal) "mean inner potential", U_{in}. The U_{in} of a solid is defined as the energy difference between vacuum level, E_{vac}, and the bottom of the valence band (yielding in average values btw. 10–16 eV). When the incoming free-electron approaches and trespasses (also when the scattered/ejected electron leaves) the solid-

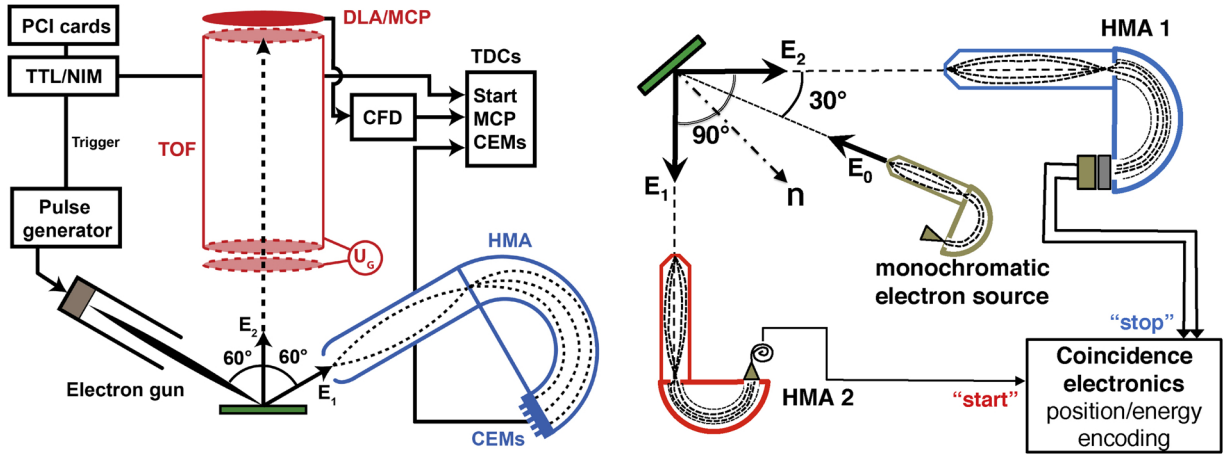

Fig. 7. Schematic view of the SE2ELCS spectrometer *(left)* at Vienna University of Technology and of the LASEC spectrometer *(right)* at the Università degli Studi Roma Tre. For SE2ELCS the trajectory of the incident electrons encloses a 60° angle with the surface normal of the sample. The HMA, equipped with 5 channeltrons, is in specular reflection and detects the reflected electrons, while the TOF-analyser is placed along the surface normal and the emitted electrons are detected with a detector consisting of Multi Channel Plates (MCP) and a Delay Line Anode (DLA). In LASEC the specimen is bombarded by a monochromatic electron beam which encloses an angle of 30° with HMA1. This latter is positioned at 90° from HMA2 within the detection plane. HMA1 is equipped with a two-stage MCP and a mono-dimensional delay line anode (1D-DLA), whereas HMA2 has a single channeltron. By varying the sample surface rotation w.r.t. both analysers a large variety of kinematics can be accessed, ranging from specular reflection conditions to higher order Bragg diffracted beams.

vacuum interface it undergoes refraction at the surface (Snell's law). The primary electron energy at which the specular peak exhibits highest intensity is chosen for the subsequent coincidence measurements. In this case, it is the fourth order Bragg peak found at 173 eV incident energy, that agrees with the expected value according to Ruocco et al. [96]:

$$E_{\mathrm{Bragg}} = \left(\frac{\hbar^2\pi^2}{2\,m_e\,d^2}n^2 - U_{\mathrm{in}}\right)\frac{1}{\cos^2\theta_i{}^{\mathrm{vac}}} \tag{6}$$

where the inner potential $U_{in} = 16$ eV, the spacing between planes $d = 3.35$ Å, θ_i^{vac} is the real angle of incidence fixed by the experiment (in vacuum) and n gives the diffraction order; other symbols have their usual meaning.

In the LASEC laboratory (sketched on the right-hand side of Fig. 7), the target is bombarded by a continuous electron beam produced by a home-built mono-chromatic electron source with an energy resolution of about 60–90 meV. Typically, during a coincidence measurement the primary current, I_0, of the electron beam is kept around 10–15 pA. The electron gun encloses an angle of 30° with HMA1 and of 60° with HMA2, hence the two analysers are positioned orthogonally to one another in the scattering plane (see also Fig. 7). The detector of the hemispherical analyser 1 is composed of a two-stage microchannel plate (MCP) and a mono-dimensional delay line anode (1D-DLA) that provides position sensitive capability. Whereas the HMA2 is equipped with a single channeltron. Coincidence measurements were performed on HOPG in specular reflection conditions for the analyser HMA2, i.e. $\theta_i = \theta_o = 30°$, which means that electron scattering events occurring along crystallographic directions in-between the two main in-plane symmetry directions of ΓK and ΓM all contribute to the (e,2e)-process. The measurements were conducted at two different primary energies, of ca. 50 eV and 90 eV. These primary energies, E_0 or E_{bragg}, satisfying Eq. (6), correspond to the fourth- and fifth-order Bragg peaks as calculated on the basis of the chosen scattering conditions.

The electron optics of either HMA is tuned to provide optimal and almost uniform transmission of electrons in the kinetic energy range of interest. The tuning was optimised for both the high energy (HE) and the low energy (LE) ranges of the electron energy spectrum. Such a specialised tuning allows to associate each analyser to detection of either "scattered" or "ejected" electrons.

Prior to launching each (e,2e)-measurement, position and rotation of the sample are optimised along with the focus and deflection of the electron beam, thus maximising the spectrometer efficiency for the chosen experiment. These fine-tuning adjustments are done on the basis of the double-differential spectra, i.e. REELS or SEES, and angular diffraction patterns, acquired right after sample preparation. For a chosen kinematics, both REELS and SEES provide information on the available excitation channels and on the accessible emission channels, respectively.

For the experiments performed using $E_0 \simeq 90$ eV analyser HMA1 was tuned to collect the SE-spectrum, whereas HMA2 (the one kept in specular reflection conditions) was dedicated to the acquisition of the Energy Loss part of the electron spectrum (ELS). For the series of (e,2e)-measurements done at 50 eV both analysers were capable of acquiring the entire electron spectrum and their role could be switched at any time. Further experimental details concerning both apparatus can be read in Refs. [95,97].

4. TEY measurements & results

Electron yields from HOPG and a-C were studied: (a) as a function of the incident electron energy E_0 and (b) in dependence of the angle of incidence, θ_i. The experiments were conducted in two different energy ranges: (a) a high-energy (HE) range comprising a primary energy interval in between ~50 eV and 1800 eV and (b) a low kinetic energy range (LE) spanning between landing energies of ~0 eV up to 50 eV.

For E_0 values exceeding 50 eV the energy-dependent TEY trend is similar for all materials and exhibits its commonly known shape (shown in Fig. 2 and in Fig. 8). At first the yield increases with E_0, reaching a maximal value σ_{max} at an impact energy $E_0^{\max}$ after which it decreases again for higher primary energies. The value of $E_0^{\max}$ at which this maximal yield is observed strongly varies with the status of the surface. In fact, the TEY is highly surface sensitive and, depending on the cleanliness and roughness of the surface the primary energy at which the σ_{max} is observed, may even change by several hundreds of eV.

For TEY measurements in the HE-range or HE-TEY (commonly known as SEY) the electron gun energy is scanned up to 1800 eV, therefore the potential difference given in Eq. (4) is negligible, since in this case the cathode potential of the electron gun exceeds the sample bias by two orders of magnitude ($U_{gun} \gg V_{bias}$, with $V_{bias} < 0$ V) and the nominal primary energy, E_0 is dominated by the electron source potential. Fig. 8 shows four HE-TEY-curves acquired from both targets at different stages of cleanliness. This was done to inquire the surface

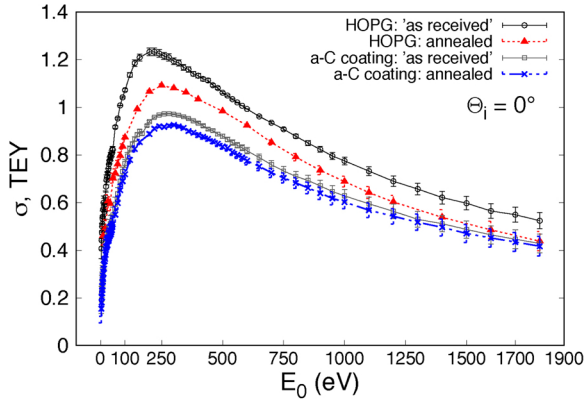

Fig. 8. Primary energy-dependent HE-TEY-curves from HOPG and an a-C coating, both measured at two different stages of cleanliness – *'as received'* and after *annealing* (see legend).

sensitivity of the electron yield. The specimens labelled 'as received' were measured right after insertion into UHV (base pressure $\sim 2 \cdot 10^{-9}$ mbar) and prior to the annealing. The 'as received' HOPG surface (black line with error bars in Fig. 8) exhibits a maximal yield at an impact energy $E_0^{max} \cong 200$ eV with a σ_{max} of ca. 1.23 (with 5% uncertainty). After annealing (red dotted line with triangles) the maximal yield decreases down to 1.08 and the energy at which it is observed increases to ca. 250 eV. For the a-C in both surface preparations stages (grey and blue lines in Fig. 8) the kinetic energy at which the maximal yield is observed does not vary and is found around 265 eV. However, the annealing process influences the intensity of the σ_{max} by lowering it from 0.97, for the 'as received' sample (grey), down to 0.91 for the clean sample (blue). These variations of the overall TEY trend, as well as the change in position and intensity of the maximal yield, observed in either case, can be undoubtedly assigned to the different status of the surface, thus emphasising the surface sensitivity of this physical parameter. Angle-dependent studies were performed on both annealed (clean) targets. In our experiments, the angle of incidence, θ_i, was varied between 0° and 21°. In case of the a-C sample (not shown) no variation of σ_{max} or of E_0^{max} (within experimental uncertainties) could be observed at any θ_i. Intensity variations of the maximal TEY-value can be also induced by a variation of the angle of incidence of the electron beam, θ_i (defined with respect to the surface normal of the sample). Commonly, σ is found to increase with increasing θ_i, since at more grazing incidence the secondary electrons are generated closer to the surface-vacuum interface thus making their escape from the solid more

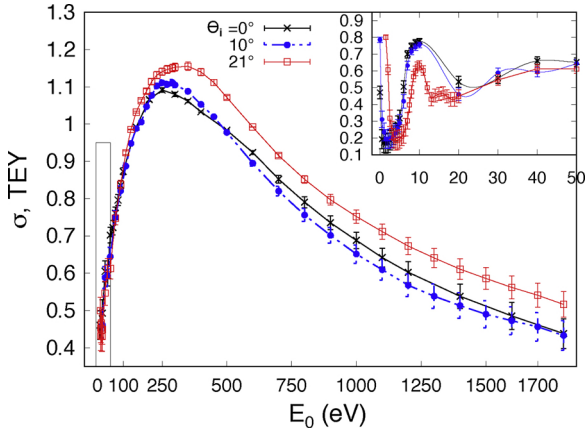

Fig. 9. HE-TEY curves of the clean HOPG surface acquired at three different θ_i *(see legend)*. The low-energy range (LE) up to 50 eV is shown enlarged in the inset and exhibits several modulations. Details on the LE-part of σ are discussed further in the text and shown in Fig. 10.

Table 1
Angle-dependent yield maxima for the annealed HOPG sample.

θ_i (°)	σ_{max} (–)	E_0^{max} (eV)
0	1.08	250
10	1.10	269
21	1.15	320

preferable [1,98,99]. An empirical formula proposed by Vaughan in Refs. [100,98] makes it possible to calculate the value of σ_{max} and to predict where to expect the E_0^{max} value, in dependence of the impact angle. Fig. 9 shows three HE-TEY curves from HOPG measured at different θ_i-values. As expected, the larger the angle of impact, the greater the yield maximum, the higher the primary energy at which the σ_{max} is observed. All measured values are given with an uncertainty of max. 1–2% in Table 1 and were found to be in reasonable accordance with those calculated using the formulas from Ref. [100,98]. In the inset of Fig. 9 the LE-range up to 50 eV is given on an enlarged scale. The observed modulations in the TEY-curve are intrinsically linked to the electronic structure of this layered crystalline surface and vary both in shape and intensity in dependence of the angle of incidence, θ_i. A more detailed description of the TEY behaviour in the LE-range is given on the basis of Fig. 10.

Fig. 10(b) shows three LE-TEY curves measured under normal incidence on both the 'as received' (black) and 'annealed' (red) HOPG surface as well as on the clean a-C coating (blue dashed). The energy scale is again defined w.r.t. the Fermi level of the apparatus. All three LE-TEY curves start with a σ of 1, indicating total electron reflection, followed by descending slopes, where respective inflection points provide values for the target workfunctions. At the descending slope of the un-annealed HOPG sample, σ drops from 1 down to 0.4. For energies ranging from ca. 5 eV up to 50 eV the LE-TEY slightly rises exhibiting some very faint modulations. Instead, at the slope of the LE-TEY measured on the annealed HOPG surface (red curve in Fig. 10), σ drops down to 0.2. and exhibits evident modulations at higher energies. The overall higher yield in the former case can be ascribed to the presence of contaminants, e.g. water, oxygen, CO. Presence of such contaminants on the surface is known to induce a strong change of the elastic

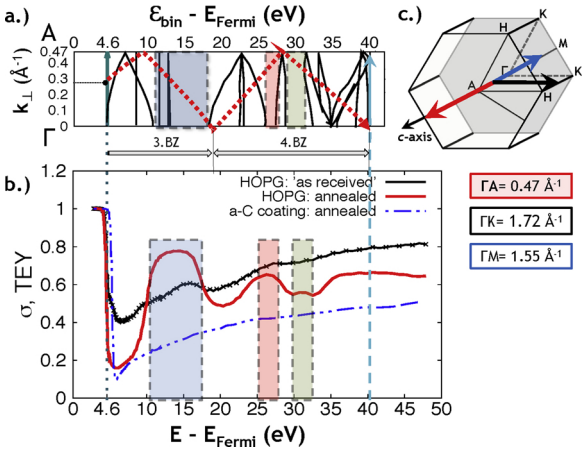

Fig. 10. *Panel (a):* Red dashed curve representing the experimental LE-TEY scan conducted on HOPG superimposed on the calculated band structure according to Ref. [89], displayed along the ΓA-symmetry direction. *Panel (b):* LE-TEY curves from the 'as received' HOPG sample (black), from the clean (after annealing) HOPG surface (red) and from the clean a-C coating (dashed blue). Coloured rectangular areas highlight regions in the E-structure of HOPG where a higher TEY-value is measured. These regions correspond to zones in the unoccupied band structure (see panel (a)) exhibiting energy gaps. *Panel (c):* Brillouin zone of graphite.

scattering at low energy [101]. For the clean HOPG sample, Φ_s amounts to 4.6 ± 0.2 eV, whereas for the a-C coating it is 5.0 ± 0.2 eV. Variations in the workfunction are expected for different crystalline orientations of the same material. Similar values for (unordered) Carbon can be found in Ref. [84].

In the following, particular attention is dedicated to the interpretation of the LE-TEY structures measured on the clean HOPG surface, for which the final-state band structure must be considered. To this end, Fig. 10(a) shows the unoccupied band structure of graphite, as calculated by Strocov et al. in Ref. [89], and given along the ΓA-symmetry direction, the direction relevant in this experiment. Energy gaps are highlighted in colour and are brought in connection with higher σ values measured on the clean HOPG surface. Fig. 10(c) depicts the Brillouin zone of graphite displaying its high-symmetry directions indicated by coloured arrows.

On the basis of current knowledge, stating that at very low energies (< 10 eV) the electron IMFP resembles the one of keV-electrons, to describe the impingement of these very LEEs on the surface, we rely on the solutions given by quantum mechanics, where the reflectivity (transmission) of electrons is treated as an incident plane wave encountering a sudden potential step [102]. Under this assumption, whenever an electron passes the solid-vacuum interface (for either side) it is refracted by the surface potential barrier.

Due to the presence of the so-called mean inner potential, U_{in}, when one of these electrons is inside the target it has a shorter wavelength, i.e. its kinetic energy increases to $(E - E_{vac} + U_{in})$. As a 0th order approximation we assume validity of the plane wave approximation, although at low energies Bloch waves can significantly differ from plane waves [90,91]. Nevertheless, in crossing the surface, conservation of energy and the parallel component of the linear momentum ($|k_{\parallel,out}| = |k_{\parallel,in}|$) hold and on this we rely in order to determine both the parallel and the perpendicular components of the momentum inside the solid:

$$|k_{\parallel,\mathrm{out}}| = |k_{\parallel,\mathrm{in}}| = \frac{1}{a_0}\sqrt{\frac{2(E - E_{vac})}{E_H}}\cdot\sin\theta_i \tag{7}$$

$$|k_{\perp,\mathrm{in}}| = \frac{1}{a_0}\sqrt{\frac{2}{E_H}[(E - E_{\mathrm{vac}})\cdot\cos^2\theta_i + U_{\mathrm{in}}]} \tag{8}$$

Inside the sample, the wavelength change only affects the perpendicular component of the wave vector. Based on this simplified approach, for each energy value $(E - E_{vac})$ scanned during the acquisition of the red LE-TEY curve, we calculate the perpendicular component of the electron momentum associated to it. The red dashed line in Fig. 10(a) represents the points in *k*-space corresponding to the energy scan shown in panel (b) as per Eqs. (7) and (8). For energies at which respective perpendicular *k*-vector values coincide with a region in phase-space entailing energy gaps (e.g. as seen between 10 eV and ~17 eV along the ΓA-symmetry direction shown in panel (a)) a rise of σ is observed. This contribution to the total yield can be ascribed to elastically reflected electrons, whose free-electron wave-function does not match any Bloch wave inside of the target, since no empty states are available in the energy gap. Such a rise in the yield can be observed in the LE-TEY energy structure for the three energy ranges highlighted by coloured rectangles. Total Current Spectroscopy and other TEY-data from the literature [88,103,50,104,89] confirm that materials exhibiting the strongest current modulations are layered structures, of which graphite (and HOPG) represents a prominent prototype.

For energies up to 50 eV, the TEY is dominated by elastically reflected and inelastically backscattered electrons [1,3,88]. Features corresponding to enhanced reflectivity η of electrons are directly linked to the band structure above the vacuum level [52,87,86,89,91], in particular to the presence of energy gaps or to strongly-localised (non-dispersing) bands. Further modulations in the TEY of a material are associated to inelastic scattering processes, such as an interband transition and to collective modes, e.g. plasmon excitations [88,89,83]. In the other intermediate energy regions, where unoccupied states are available, the electron manages to penetrate into the target – since in this case its wave function couples with a Bloch wave function of the crystal – and interaction with solid-state electrons eventually induces emission of SEs. In these energy regions of the sampled band structure, a rise of the σ is more likely to be linked to SEE. These available unoccupied energy bands represent accessible channels through which generated SEs manage to escape above vacuum. Similar findings were described and analysed in depth by authors of Refs. [89,91]. The relevance of the unoccupied band structure in the SE-emission process becomes particularly evident when measuring (e,2e)-coincidence spectra (see Section 6). In conclusion, the LE-TEY energy structure of HOPG gives an ideal example for how these modulations are intimately linked to the interplay between reflection of electrons at the surface and their transmission through the target, yielding eventually to the emission of SEs.

The LE-TEY of the a-C, given in Fig. 10(b) as dashed blue curve, does not exhibit any modulation at all. Firstly, in case of the amorphous C coating, the inflection point of its descending slope yields a noticeably higher workfunction value. As explained in Section (3.1) these changes in workfunction can be expected for different allotropes of a same material. The overall trend of the LE-TEY curve does not exhibit any noticeable features and grows monotonically for increasing landing energy. This is expected, since the electronic structure of this Carbon allotrope has no definite direction in reciprocal space, hence all possible crystalline directions will contribute to the diffusion of the landing electrons.

Disappearance of modulations in LE-TEY curves of HOPG were observed by Gonzalez et al. in Ref. [105] after sputtering the sample – hence leading to a disruption of its structural order – yielding a similar LE-TEY curve as obtained in case of the a-C coating.

5. Theoretical background for the interpretation of (e,2e)-coincidence spectra

To gain full control on the statistical, macroscopic process, that generates secondary electrons, the individual interactions must be properly understood and modelled. In essence, the individual events at stake are ionising electron collisions with the solid, these being the interactions that multiply the incoming flux of electrons by a factor two, at least. Over the past fifty years, (e,2e)-coincidence spectroscopy has established itself as a much useful tool in unraveling the electron impact mechanism in atoms, molecules, solids and for impact energies ranging from several keV down to ionisation threshold [106].

In an (e,2e)-experiment performed on a solid, an electron beam with well-defined kinetic energy and momentum (E_0, $\vec{k}_0$) is brought to collide with the solid surface and, as a result of the ionising collision, a pair of time correlated unbound electrons (in the following labelled “s”, for *scattered*, and “e” for *ejected*) is generated. Those pairs that abandon the solid are detected coincident in time, their energy and momentum, (E_s, $\vec{k}_s$) and (E_e, $\vec{k}_e$), are measured with a given probability for them to be emitted into the two solid angles $\Omega_s(\theta_s, \phi_s)$ and $\Omega_e(\theta_e, \phi_e)$. Such an experiment, where the kinematics under which the process takes place is fully determined, allows to unambiguously determine the parameters that are relevant in determining the differential (in energy and angle) probability for the ionisation to happen, i.e. the energy $\Delta E = E_0 - E_s$ and the momentum $\Delta\vec{K} = \vec{k}_0 - \vec{k}_s$ transferred in the collision. Within this schematic description the ejected electron, described by the wave function $\psi_e(E_e, \vec{k}_e)$ plays the role of a “*secondary*” electron thus establishing a direct proportionality between the Triple-Differential Cross-Section (TDCS) for electron pairs generation and the probability of generating secondaries, with well defined energy and momentum, in an individual collision. The differential cross section is readily calculated within first-Born approximation and it can be subdivided in a kinematical factor, related to the three electron momenta and mostly

independent from the target properties, times a form factor that is entirely linked to the electronic structure of the target [107]:

$$\frac{d^3\sigma}{d\Omega_s d\Omega_e \mathrm{d\,E}} \propto \left(\frac{\vec{k_s}\cdot\vec{k_e}}{\vec{k_0}}\right) |\,\bar{F}_{\mathrm{if}}\,|^2 \tag{9}$$

The form factor $|\bar{F}_{\mathrm{if}}|^2$ assumes an easy to compute form in two limiting cases [108]:

(a) in the *dipolar limit*, i.e. when the energy transfer is small with respect to E_0 and the inverse of the momentum transfer is small with respect to the dimension of the electron orbital involved in the collision (valid roughly for momentum transfers up to 1 $Å^{-1}$)

$$|\,\bar{F}_{\mathrm{if}}\,|^2 \propto \frac{1}{\Delta\vec{K}^4} |\,\langle f\,|\sum_i \exp^{i\Delta\vec{K}\cdot\vec{r_i}}|\,i\rangle\,|^2 \tag{10}$$

where $|\,i\rangle$ and $|\,f\rangle$ are the *n*-electrons initial and final states and $\vec{r_i}$ is the *i*th electron coordinate

(b) in the *binary limit*, where large energy and momentum transfers are considered (a few $Å^{-1}$) yielding a form factor as given below

$$|\,\bar{F}_{\mathrm{if}}\,|^2 \propto \mathbf{M}^2\,|\,\langle k_1\cdot f\,|\,k_0\cdot i\rangle\,|^2 \tag{11}$$

where **M** is the free-electron scattering matrix element and it further simplifies upon validity of the impulse approximation for the collision and for the independent particle description of the target. In the frozen core limit, the wave functions of the $(n-1)$-electrons (not involved in the ionisation) are factored out of the Coulomb interaction matrix element yielding a monopole matrix element, whose modulus squared is termed Fractional Parentage Factor ($\mathcal{R}_{i,f}$) that represents the probability for the initial neutral state to be projected on the final ionic state. Eq. (11) then becomes

$$|\,\bar{F}_{\mathrm{if}}\,|^2 \propto \mathbf{M}^2\,|\,\phi_n(\vec{q},\,\varepsilon_n)\,|^2\cdot\mathcal{R}_{i,f} \tag{12}$$

being $|\,\phi_n(\vec{q},\,\varepsilon_n)\,|^2 = \rho_n(\vec{q},\,\varepsilon_n)$ the momentum density of the initial *n*th independent particle occupied state – i.e. the density of occupied states of the initial (neutral) state given as a differential of the momentum $\vec{q}$. The *n*th-electron state that contributes to the form factor satisfies energy conservation law as follows:

$$\varepsilon_n = E_e - \Delta E + \Phi \tag{13}$$

where ε_n is the binding energy of the *n*th-state with respect to the Fermi level and Φ is the sample work function. The momentum $\vec{q}$ can be assimilated to the crystal momentum of the initial *n*th-state and is determined by the momentum conservation law, displayed here below separated into its parallel ($\|$) and perpendicular ($\perp$) components:

$$\vec{q}_{\|} = \vec{k}_{e,\|} - \Delta\vec{K}_{\|} + \vec{G}_{\|} \tag{14}$$

$$q_{\perp} = k_{e,\perp} - \Delta K_{\perp} + G_{\perp} \tag{15}$$

As previously explained in Section (3.3) the parallel component of the momentum is conserved upon the surface-vacuum boundary, whereas the perpendicular component inside the solid is changed due to refraction at the interface. The $\vec{G}_{\|,\perp}$ is the sample crystal reciprocal lattice vector for a given symmetry direction. This interpretation of the (e,2e) events directly links the threefold differential cross section with the target electronic structure and likewise the yield of the secondary electrons is intimately linked to the target electronic structure. This framework of description of an (e,2e)-event has proven to be quite robust for what concerns the energy at which the experiment is performed, from 20 keV [109] to 300 eV [110], the aggregation state, from single crystal [109] to amorphous [111], the kinematics, from transmission through thin films [109] to reflection from clean surfaces [110].

In this work (e,2e)-events are used to gather information on the elementary mechanism of secondary electron generation in the energy regime below 200 eV and, due to the shortness of the mean free path at this energies, the only viable geometry for the experiment is a reflection geometry, i.e. the final electron pair and the incoming beam are on the same side of the solid surface. The first such an experiment was realised over twenty years ago [43,112] at very low incident energies ($\approx$20 eV) and gave the unique chance to study the dynamics of direct electron collisions a few electronvolts above the vacuum level, thus physically discriminating between direct impact and cascade ionisation events. A few years later, it was demonstrated [113] that for incident energies well above the vacuum level, the direct impact regime is expected to dominate the (e,2e) cross section in reflection geometry thus providing a "portrait" of the electrons moving in the bound state that is unique to other kind of electron spectroscopies. The model adopted and successfully applied till now for this latter kind of experiments is based on the First Born Approximation (FBA) [46]. The incident electron is described as a plane wave, whereas the target electrons, initial and final states, are described by one-electron Bloch wave functions in the momentum space representation. In analogy to what is done in the three step model in photoionisation from solids, the ejected electron wave function within the solid, $\psi_e(E_e,\,\vec{k_e})$, matches the energy and the parallel momentum component of the corresponding plane wave in the vacuum. For moderate incident energies and for low energy of the ejected electron, confining the interaction model to within FBA and using plane waves for the ejected (secondary) electrons in vacuum, the (e,2e) cross section is [113,114]:

$$\frac{d^3\sigma}{d\Omega_s d\Omega_e \mathrm{d\,E}} \propto \left(\frac{\vec{k_s}\cdot\vec{k_e}}{\vec{k_0}}\right)\frac{1}{\Delta\vec{K}^4}\,\frac{1}{\varepsilon(\Delta\vec{K},\,\Delta E)}\sum_{\psi_e}\rho_n(\vec{q},\,\varepsilon_n)\,|\,C_{\psi_e}(\vec{k_e})\,|^2\,\delta_{\vec{q}+\Delta\vec{K},\vec{k_e}} \tag{16}$$

With the summation extended to all terms of the Bloch expansion of the ejected electron wave function [114] and with the Dynamical Screening Function $\varepsilon(\Delta\vec{K},\,\Delta E)$ that accounts for Coulomb screening effects and collective excitations of the medium in which the ionisation takes place. This function is analogous to the dielectric function and is linked to the Coulomb screening length. It is therefore intrinsically connected to plasmon excitations (see also [115]).

In Eq. (16) the $C_{\psi_e}(\vec{k_e})$ are the coefficients of the Bloch wave expansion for the ejected electron. They are directly linked to the unoccupied DoS towards which the ionised electron is promoted by the energy and momentum transferred in the collision. Only in the limit of large E_e (> 20 eV) this coefficient becomes unity, when it is admissible to describe the ejected electron wave-function as a plane wave. In this case the summation over ψ_e reduces to a single term.

It is at this point evident that for the emission of a secondary electron to happen, energy and momentum conservation should allow a transition from an initial occupied state to a final unoccupied state. While for secondaries with sufficiently high kinetic energies (> 20 eV) it is likely to be ejected, since the unoccupied DoS monotonously increases towards the continuum, for SEs with kinetic energies $\leq$20 eV emission is only possible when empty bands are accessible. In this energy LE-range, in fact, the DoS of the unoccupied bands cannot be disregarded and its structure modulates the (e,2e)-yield. The probability for the allowed transition is determined by the joint initial-final state momentum density and is modulated by the dielectric function, or alternatively by the screening length.

Several dynamical models have been suggested for accounting a reflection kinematics for the (e,2e) process [116], but at present the most accredited is the one applied by Iacobucci et al. [113,46] that is based on an elastically assisted inelastic collision originally proposed by Diebold et al. [117] and definitively demonstrated to be the dominant one by Ruocco et al. [96]. In this mechanism – Diffraction-Loss or "DL" model – the projectile either reflects specularly from the surface or diffracts from the target lattice and subsequently undergoes an inelastic collision (Fig. 11).

Both (e,2e) [46] and elastic-inelastic diffraction [48] experiments support the description of the ionising collision as happening inside the

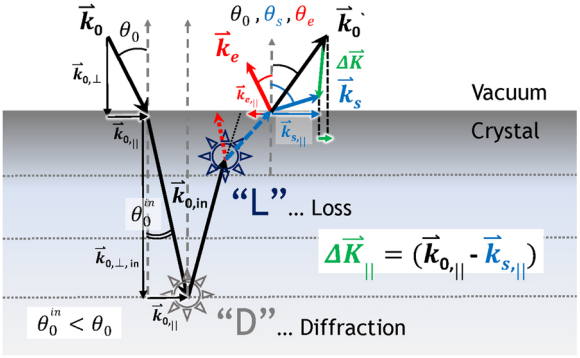

Fig. 11. Schematic illustration of the "DL"-scattering process. The incoming electron with primary energy, E_0, and momentum $\vec{k}_0$ penetrates the crystal surface and undergoes refraction influenced by the inner potential, U_{in}. It then suffers an elastic scattering towards the surface by Bragg reflection (*diffraction* process: "D") where its momentum is mirrored. During its path towards the surface it experiences an inelastic collision, wherein part of its energy (ΔE) and momentum ($\Delta\vec{K}$) are transferred to the solid-state electrons. During this inelastic scattering event (or *loss* process "L"), the direction of the scattered electron is only slightly changed with respect to the elastically reflected beam. The energy is transferred to a bound electron, that if manages to escape is then detected as SE with E_e and $\vec{k}_e$. In "DL"-scattering the loss process is assisted by an elastic collision, thus the resulting momentum transfer remains very small. (More details can be found in [46,97]).

solid, hence the trajectories of the three unbound electrons (incoming, scattered and secondary) are refracted by the inner potential barrier in entering and exiting the sample surface. Inside the solids the incoming electron undergoes diffraction from the crystal lattice (the specularly reflected beam is a 0th-order diffraction). Each diffracted beam acts as a primary beam for the following ionising collision, whose cross section decreases rapidly with increasing momentum transfer (see Eq. (16)). Consequently, all correlated pairs emerging from the surface are predominantly generated by diffracted beams pointing towards the surface and the (e,2e) events in reflection geometry are equivalent to events generated in transmission geometry by monocromatic electron beams generated within the solid by diffraction. Due to the sharp dependence of the cross section on the momentum transfer (i.e. the scattering angle), almost the totality of the single scattering (e,2e) events happens with the primary electron scattered along the diffraction/reflection direction and most of the plural scattering in the vicinity of it (within a few degrees opening angle at the energies of the present experiments).

This two-step mechanism dominates over the one-step one, a single inelastic scattering, because it minimises the momentum transfer hence maximising the (e,2e) cross section, as it is inversely proportional to the forth power of the momentum transfer. The conjugate process, in which the inelastic ionising scattering takes place first and the two electrons are refracted afterwards from the crystal, is not to be considered separately since it is described by the same formulas of the process in which the ionisation is preceded by the diffraction, at least as long as the experiment is performed in specular reflection.

6. (e,2e)-Coincidence measurements & results

The results of (e,2e) coincidence measurements taken in the SE2ELCS spectrometer are shown in Fig. 12 for HOPG (left) and glassy Carbon (right). Both (e,2e) experiments were performed under identical measurement conditions: each surface was bombarded by a primary electron beam of 179 eV (w.r.t. E_{Fermi}) under specular reflection conditions. Each pixel in the double-differential maps shown in Fig. 12 represents a *correlated* electron pair composed of a *scattered* electron with energy E_s above the Fermi level (indicated along the ordinate axis) and of an *ejected* electron with kinetic energy E_e above the vacuum level (co-ordinate axis). The (e,2e)-spectra are overlaid with reflection electron energy loss spectra (white line) measured on the respective targets at the same incident energies and under the same kinematical conditions as the underlying double-differential (e,2e)-coincidence data. The (e,2e)-yield intensity (indicated by the colour scale) represents the probability for the ejected electron to be emitted as a result of an inelastic scattering experienced by the primary electron, which undergoes a corresponding energy loss ($\Delta E = E_0 - E_s$) during the collision. Such double-differential (e,2e)-spectra therefore provide a causal connection between the energy losses and emitted SEs. Furthermore, in (e,2e)-coincidence experiments the energy dissipation and the momentum transfer processes occurring during an interaction can be studied simultaneously to the SE-emission process since both initial and final states are predetermined. In the REELS spectra (white lines), the most intense peaks are given by the elastically reflected electrons. The sharpest loss features are due to single inelastic scattering. A first sharp feature is visible at $(E_s - E_{Fermi}) = 168.2$ eV or $\Delta E = 6.2$ eV for HOPG and at $(E_s - E_{Fermi}) = 170.3$ eV or $\Delta E = 4.1$ eV for gl-C. This corresponds to an energy loss commonly attributed to a π plasmon excitation or also to the inter-band (π–π^*)-transition. A second spectral feature corresponds to the ($\pi + \sigma$) plasmon excitation ($E_s - E_{Fermi} = 151.6$ eV or $\Delta E = 22.8$ eV and $E_s - E_{Fermi} = 146$ eV or $\Delta E = 28.4$ eV) respectively [117,118,69]. Both spectral features are due to a single inelastic process and delimit what will be referred to as the single scattering region below. The π plasmon dominates the singles energy loss spectrum in HOPG, whereas it becomes manifestly less prominent in the case of glassy Carbon, where the more notable loss feature is then given by the ($\pi + \sigma$) plasmon. Spectral intensity at higher losses, or equivalently at lower E_s energies, arises mostly due to electrons participating in multiple inelastic collisions. Both HOPG spectra – the REELS and the (e,2e) coincident spectrum – exhibit an evidently diminished multiple scattering contribution with respect to the case of gl-C. Furthermore, in the REELS spectrum of HOPG, it is possible to discern the double π-plasmon excitation at $(E_s - E_{Fermi}) = 162$ eV or $\Delta E = 12.4$ eV, which constitutes further evidence for the cleanliness and well-ordered crystalline structure of the sample, as well as the proper alignment of the target along the specific crystalline symmetry directions. Constructive interference of the scattered electron waves, as achieved in Bragg-condition can strongly reinforce the signal in the detected direction, thus spectral features are enhanced and can be distinguished more easily from the inelastic background signal of multiple scattering.

The red diagonal line (in Fig. 12) indicates the Fermi level as a result of energy conservation (as given in Eq. (13)). In coincidence spectra no intensity can be observed above this "Fermi diagonal", since no electrons can be ejected with kinetic energies exceeding the energy lost by the impinging electron. Intensity appearing along this diagonal belongs to electron pairs, where the ejected electron is emitted with the full energy loss, ΔE, of the scattered primary after having overcome the target surface barrier, promoting *one* single electron above the vacuum level to accessible empty states. When comparing the singles and the coincident electron spectra in Fig. 12 a remarkable feature can be observed at the energy loss characteristic for the π plasmon. While the π plasmon is one of the strongest features in REELS there is no intensity in the (e,2e)-coincidence data. Whereas in the distribution of coincidences in either C allotrope of Fig. 12, at the characteristic energy loss for the ($\pi + \sigma$) plasmon there is a strong correlation between the ejected SEs and scattered electrons (with energies $E_s - E_{Fermi} \approx 140$–$160$ eV) showing up as a ridge-like structure distributed nearly parallel to the energy conservation diagonal.

The energy correlation for electron pairs along this spectral feature is readily explained on the basis of Eq. (13) and proves that electron emission must occur as a result of a single electron process, since there is no conceivable energy sharing mechanism leading to the observed ridge-like feature if more than one electron is ejected in the course of the same process [72]. The high (e,2e)-intensity in the single scattering region suggests that the ($\pi + \sigma$) plasmon is a relevant mechanism for the SEE-process. For the kinematics in SE2ELCS the (e,2e)-yield of

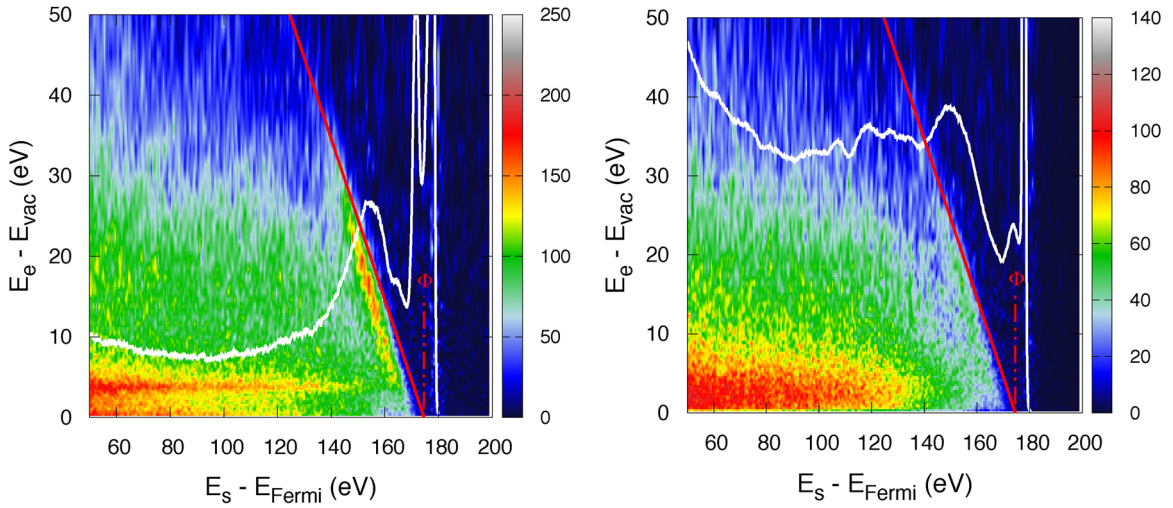

Fig. 12. (e,2e)-coincidence spectra of HOPG (left) and gl-C (right) superimposed by their respective REELS spectra (white) measured under the same kinematical conditions. Red diagonals indicate the Fermi level. The intersection of this diagonal with the ordinate axis yields the value of the sample workfunction Φ_s. The (e,2e)-yield intensity just below this diagonal corresponds to correlated electron pairs, of which the SE is ejected with $E_e = \Delta E - \Phi_s$ and the scattered electron is detected with $E_s = E_0 - \Delta E$. A ridge-like feature seen along the Fermi diagonal (for $140\,eV \leq \Delta E \leq 160\,eV$) corresponds to correlated electron pair emission obtained in the course of a single scattering event of which the energy loss corresponds to a ($\pi + \sigma$) plasmon excitation in bulk graphite. Intensity observed for higher energy losses $E_s - E_{Fermi} = (50–140)\,eV$ is attributed to multiple scattering.

HOPG along the ridge-like single scattering feature is much higher than in the case of gl-C. This is not surprising since the electronic structure of gl-C corresponds to an angular average of the crystalline structure of HOPG, leading to a diminished TDCS within the single scattering regime, but to a higher (e,2e)-yield in correspondence of the multiple scattering region.

To explain the complete absence of (e,2e)-events at the energy of the π plasmon, it does not suffice to account only for energy conservation, but also momentum conservation needs to be considered, as given in Eqs. (14) and (15). As explained in Section (5), by performing the (e,2e) experiment under specular reflection conditions it is possible to additionally exploit coherent elastic scattering to obtain a stronger signal in the direction of detection, which in case of the ordered target (HOPG) also results in a fully momentum-resolved measurement. Owing to momentum conservation, determining the parallel component of the momentum transfer ($\Delta\vec{K}_{||}$) occurring during the interaction yields the in-plane momentum component of the bound electron ($\vec{q}_{||}$) prior to its emission. Since the experiments were performed in specular reflection geometry, both in-plane symmetry directions of ΓM, ΓK and all in between crystalline directions in the electronic structure of graphite contribute to the diffusion of electrons during a collision and therefore energy bands in all directions need to be considered as available initial states.

To obtain the full picture of the electron-solid interaction measured during a coincidence experiment it is advantageous to indicate the resulting (e,2e)-yield as a function of the initial state of the bound electron prior to its emission above the vacuum level, i.e. indicating the intensity of each correlated electron-pair associated to a ($\vec{q}_{||}$, ε_{bin})-value for the bound electron, calculated on the basis of Eqs. (13) and (14). Fig. 13 shows the combined (e,2e)-cross sections from HOPG resulting from experiments performed in the SE2ELCS and the LASEC spectrometers and displaying the subset of coincidence measurements sharing common values of binding energies. In Fig. 13 the (e,2e)-intensity (in colour scale) represents the probability for a bound electron to be promoted above the vacuum level, when a specific inelastic collision, defined by the kinematics of the experiment, occurs. The different kinematics used in both experiments allow to cover nearly the complete first Brillouin zone of graphite, whose relevant in-plane symmetry directions of ΓM and ΓK of the initial state (below Fermi level) are shown as white lines superimposed on the (e,2e)-yield displayed in Fig. 13.

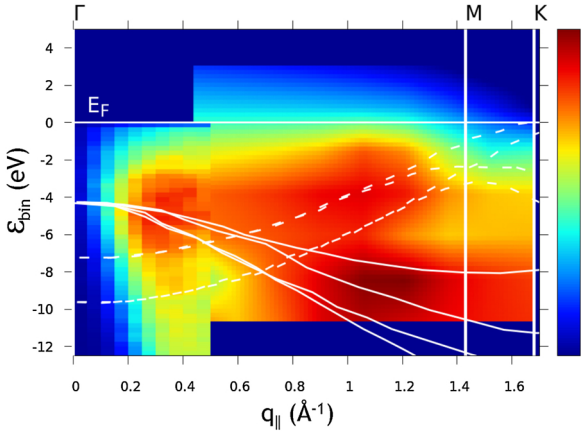

Fig. 13. Combined (e,2e)-yield from HOPG measured using both experimental set-ups shown in Fig. 7.

The $\pi_{1,2}$-bands are given as dashed lines whereas the $\sigma_{2,3}$-bands as continuous lines. The representation of a measured (e,2e) data set as shown in Fig. 13 enables to bring to the fore the role played by the electronic structure of the target – in particular the role played by the *initial* state – in the SEE-process (see also Section (5)).

The regions in phase-space sampled by the SE2ELCS spectrometer (same data as shown in the left panel of Fig. 12) comprise $\vec{q}_{||}$-values for the bound electron ranging from the Γ-point up to ca. 0.5 $Å^{-1}$, whereas in the (e,2e) experiments performed in the LASEC laboratory the sampled region ranges from ca. 0.5 $Å^{-1}$ to the K-point (with $\vec{q}_{||} = 1.7\,Å^{-1}$). The combination of the two measurements allows to obtain the *coincident* SE-yield for the complete first Brillouin zone down to a maximal (common) binding energy of ca. −12 eV. The combined data set exhibits highest (e,2e)-intensity along occupied initial states. The energy and the momentum transferred during the collision induce the promotion of a bound electron above the vacuum level, whose ($\vec{q}_{||}$, ε_{bin})-values match an occupied energy band within the achievable energy and momentum resolutions (of ca. 2.56 eV and 0.25 $Å^{-1}$ respectively). The measured (e,2e)-yield intensity observed for a given occupied band is proportional to its Density-of-States (DoS) and, as will become evident in the following, to the probability for an electronic

inter-band transition to occur (see also Eq. (16)).

At the π plasmon loss, ΔE ≈ 6 eV in HOPG, the only possibility to promote any electron from the valence to the conduction band involves occupied bands at very small binding energies ($\varepsilon_{bin} \leq$ -1.5 eV). For these binding energies the only available occupied bands are the $\pi_{1,2}$-bands near the K-point, where it is known that the DoS is negligibly small [119]. For the scattering geometry used in SE2ELCS, which samples regions in the ($\vec{q}_{||}$, ε_{bin})-phase-space in between Γ and $|\vec{q}_{||}| \leq 0.5$ Å^{-1}, there are no occupied bands available at the afore-mentioned small binding energies involved in a π plasmon excitation. This explains the complete lack of intensity in the SE2ELCS spectra (left panel of Fig. 12) at ΔE-values corresponding to this characteristic loss.

The (e,2e)-kinematics achievable in the LASEC laboratory allows to sample regions in phase-space extending from the K-point down to the σ_1-energy band (this latter not shown in Fig. 13). The combined (e,2e)-cross section of Fig. 13 exhibits a significant intensity drop exactly at the K-point confirming that the occupied DoS modulates the (e,2e)-yield. The experimental TDCS as displayed in Fig. 13 enables to study the role of the *initial* state, i.e. of the occupied band structure in the SE-emission process.

As explained in Section (5), especially in the LE-regime (for energies ≤ 20 eV) the availability of empty bands is a necessary requirement for the ejected electrons to escape into vacuum through an existing empty state, i.e. performing an allowed interband transition. Therefore, together with the DoS of the occupied bands, the DoS of these empty bands additionally influence the (e,2e)-yield.

A further series of (e,2e)-measurements was carried out in the LASEC laboratory in order to specifically investigate the role played by the unoccupied band structure in the SE-emission process. Two (e,2e)-measurements on HOPG were conducted to measure the overall (e,2e)-intensity for the case when the initial state was kept constant while combining it with two different final states. The experiments were planned according to the "DL"-scattering geometry, thus assuming only one inelastic scattering event. Supported by diffraction arguments it is possible to predict (or reconstruct) the complete kinematics of the interaction, thus obtaining fully energy and momentum resolved results, for which one can purposely choose and fix both initial and final states. To set up the kinematics of an (e,2e)-experiment, we routinely made use of simulations to predict the regions of sampling in the ($\vec{q}_{||}$, ε_{bin})-phase-space achievable for specific initial and final states

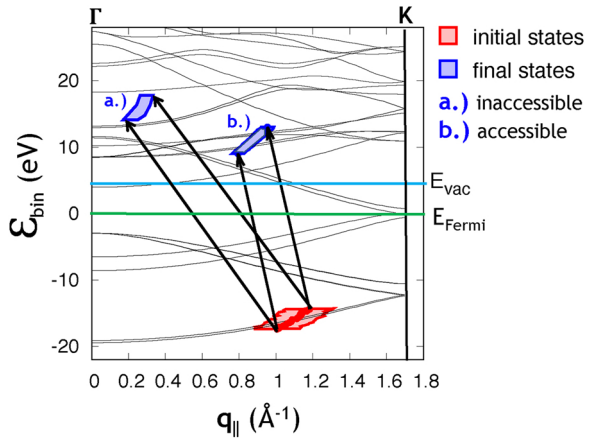

Fig. 14. Simulation of the kinematics used in two distinct (e,2e)-coincidence experiments conducted in the LASEC laboratory under the assumption of one single scattering event. These simulations were employed to predict regions of sampling with the first Brillouin zone of graphite (shown here along the ΓK-symmetry direction) for both initial (below E_{Fermi}) and final (above E_{vac}) states. The initial state (indicated by the red polygon) is fixed and identical for both experiments. The kinematics is varied by considering different momentum transfers, i.e. different energy loss processes, through which two different final states (blue polygons) can be accessed.

[97,120,34]. An example for such a simulation is shown in Fig. 14, which illustrates the two experiments performed to investigate the (e,2e)-coincidence yield in dependence of different final states. Fig. 14 shows the band structure of graphite [121] from the bottom of the valence band ($\varepsilon_{bin} = -22$ eV) up to +30 eV above the Fermi level (green line). In these two experiments, the ejected electron originates from the same initial state indicated by the red polygon in Fig. 14, thus sampling from the lowest occupied energy band, σ_1, which accoring to the authors of Refs. [111,114] exhibits the highest momentum density – the $\rho_n(\vec{q}, \varepsilon_n)$ from Eq. (16) – in the valence band. The kinematics for each experiment was varied to access the two different regions of final states characterised by (E_e, $\vec{k}_e$) for the ejected electron. The two final states chosen in these experiments are sketched as blue polygons, labelled "(a)" and "(b)" in Fig. 14 above the vacuum level (lightblue line). Shape and area of either polygon is defined by experimental acceptances. The (e,2e) experiment combining the initial state with the final state labelled with the letter "(a)" gave no (e,2e)-intensity. Due to the presence of an energy gap in the conduction band, there is no accessible empty energy band within polygon "(a)" for the ejected electron, thus the cross section for SEE vanishes. In other words, in spite of the availability of an initial state, if the momentum transfer is such, that no available unoccupied energy band can be reached, no electron can be promoted above the vacuum level. The area delimiting final states comprised within polygon "(b)" encompasses several empty energy bands. In this case, electrons originating from the occupied σ_1-band can be transferred above the vacuum level, thus their emission resulted in a contribution to the measured (e,2e)-intensity. Where availability of unoccupied energy bands is granted, interband transitions are possible. The probability for the occurrence of such an event is additionally modulated by the density of momentum ($\rho(\vec{q})$) of the considered initial and final states and is ultimately moulded by the joint density of these selected momenta [111,114]. By means of these two (e,2e)-coincidence experiments it could be assessed that – especially when considering low kinetic energies – SEE is strongly dependent on the electronic structure of the irradiated target. Availability of both initial and final states is a necessary requirement to grant the promotion of a bound electron above vacuum level, thus for it to contribute to the TDCS.

By displaying (e,2e)-coincidence spectra as a function of the scattered and ejected electron energies (as done in Fig. 12) it was possible to immediately identify the excitation of a (π + σ) plasmon as one fundamental mechanism intrinsically relevant to the generation and emission of SEs in C allotropes. By representing the TDCS as a function of the initial (and final) state, as shown in Fig. 13, it becomes possible to identify which electron energy bands are involved in the interaction, i.e. from which occupied bands electrons are ejected and promoted to available empty bands.

(e,2e) intensity observed within the single scattering ridge-like feature in the double-differential (e,2e) spectrum of HOPG is therefore directly linked to secondaries emitted in correspondence of a (π + σ) plasmon loss and which escape above vacuum level through alternate pairings of available initial and accessible final states. Based on the elastically-assisted inelastic scattering model, the (e,2e)-cross section is essentially modulated by the kinematical factor, by the selection rules defining the possibility for a given interband transition to occur as a result of the inelastic scattering event and ultimately by the form factor given in Eq. (12), which is in essence given by the density of momentum for the considered initial and final states. The present results clearly support validity of Eq. (16) as an effective way to describe elementary interactions yielding secondary electron emission, where plasmon-assisted events constitute a fundamental process.

7. Conclusions

Incoherent elastic scattering, IMFP and DIIMFP are the pillars for current MC based SE-simulation codes, but this work demonstrates that

for crystalline solids such a simple model is unable to explain features observed experimentally. In fact, these models do not account for the long-range order of solids, hence their description of electron scattering and transport is inadequate for crystalline surfaces, where interference effects play a relevant role.

The scrutinising strategy adopted in this work enabled to study the SEE-process under different perspectives, making it possible to unearth the fundamental interaction processes, as well as the other main ingredients – i.e. the electronic structure – that need to be considered when attempting a complete description of SE-emission.

Measurements of the Total Electron Yield in the LE-regime demonstrate that the band structure above the vacuum level strongly modulates the flux of both the incident electron and of the ejected electron. It is found that the TEY-response of a material is constituted by the *interplay* of reflectivity (η) and emissivity (δ) of the target.

We employ coherent elastic scattering (diffraction) to perform fully momentum resolved measurements of SE-generation on targets in a reflection geometry. By means of (e,2e)-coincidence spectroscopy it is possible to correlate excitations occurring during the electron-solid interaction with the resulting SE-features. It is found that the elementary mechanism involves the transfer of energy and momentum to one single bound electron which is promoted above vacuum level always involving the “assistance” of a plasmon loss (i.e. excitation and decay). In particular, the (e,2e)-cross section of HOPG measured in dependence of different final states has undoubtedly demonstrated the essential role played by the target electronic structure in the SEE-process. The observed (e,2e)-coincidence spectra show intensity only when the existence of both initial and final states is granted and match the corresponding energy and momentum transfers.

Acknowledgments

Financial support by the FP7 People: Marie-Curie Actions Initial Training Network (ITN) SIMDALEE2 (Grant No. PITN 606988) is gratefully acknowledged. We also thank Holger Neupert and Marco Sbroscia for their expert assistance, which was decisive for the experimental work, and Stefano Iacobucci, Francesco Offi and Pier Francesco Riccardi for stimulating discussions.

References

[1] H. Seiler, Secondary electron emission in the scanning electron microscope, J. Appl. Phys. 54 (11) (1983) R1–R18.
[2] J. Scholtz, D. Dijkkamp, R. Schmitz, Secondary electron emission properties, Philips J. Res. 50 (3) (1996) 375–389, https://doi.org/10.1016/S0165-5817(97)84681-5 new Flat, Thin Display Technology, http://www.sciencedirect.com/science/article/pii/S0165581797846815.
[3] A. Shih, J. Yater, C. Hor, R. Abrams, Secondary electron emission studies, Appl. Surf. Sci. 111 (1997) 251–258.
[4] J. Wiza, Microchannel plate detectors, Nucl. Instrum. Methods 162 (1979) 587, https://doi.org/10.1016/0029-554X(79)90734-1.
[5] J. Wiza, Sensors, Optical Sensors, John Wiley & Sons, 2008.
[6] M.A. Gusarova, V.I. Kaminsky, L.V. Kravchuk, S.V. Kutsaev, M.V. Lalayan, N.P. Sobenin, S.G. Tarasov, Multipackting simulation in accelerating rf structures, NIMA 599 (2009) 100–105, https://doi.org/10.1016/j.nima.2008.09.047.
[7] R. Cimino, T. Demma, Electron cloud in accelerators, Int. J. Mod. Phys. A 29 (2014) 1430023.
[8] G. Rumolo, F. Ruggiero, F. Zimmermann, Simulation of the electron-cloud build up and its consequences on heat load, beam instability and diagnostics, Phys. Rev. Lett. ST Accel. Beams 4 (2001) 012801.
[9] G. Rumolo, H. Bartosik, E. Belli, P. Dijkstal, G. Iadarola, K. Li, L. Mether, A. Romano, M. Schenk, F. Zimmermann, Electron Cloud Effects at the LHC and LHC Injectors, IPAC2017, (2017).
[10] O. Brüning, L. Rossi, The High Luminosity Large Hadron Collider, WORLD SCIENTIFIC, 2015, https://doi.org/10.1142/9581.
[11] G. Skripka, G. Iadarola, Beam-Induced Heat Loads on the Beam Screens of the Inner Triplets for the hl-lhc, CERNacc, (2018) https://cds.cern.ch/record/2305245/files/CERN-ACC-NOTE-2018-0009.pdf.
[12] B. Henrist, N. Hilleret, M. Jimenez, C. Scheuerlein, M. Taborelli, G. Vorlaufer, Secondary electron emission data for the simulation of electron cloud, ECLOUD'02: Mini-Workshop on Electron-Cloud Simulations for Proton and Positron Beams, CERN, Geneva, Switzerland, 15–18 April 2001: Proceedings, 2002, pp. 75–78 http://cern.ch/conf-ecloud02/papers/allpdf/hilleret.pdf.
[13] H.B. Garrett, A.C. Whittlesey, Guide to Mitigating Spacecraft Charging Effects, Wiley-Blackwell, 2012.
[14] H.B. Garrett, A.C. Whittlesey, Introduction, Wiley-Blackwell, 2012, pp. 1–5, https://doi.org/10.1002/9781118241400.ch1 (Ch. 1).
[15] J. Dever, B. Banks, K. de Groh, S. Miller, Chapter 23 – degradation of spacecraft materials, in: M. Kutz (Ed.), Handbook of Environmental Degradation of Materials, William Andrew Publishing, Norwich, NY, 2005, pp. 465–501, , https://doi.org/10.1016/B978-081551500-5.50025-2 http://www.sciencedirect.com/science/article/pii/B9780815515005500252.
[16] Z. Němeček, J. Pavlu, I. Richterová, J. Šafránková, J. Vaverka, Secondary electron emission and its role in the space environment, AIP Conference Proceedings (1925).
[17] G. Fubiani, H.P.L. de Esch, A. Simonin, R.S. Hemsworth, Modeling of secondary emission processes in the negative ion based electrostatic accelerator of the international thermonuclear experimental reactor, Phys. Rev. ST Accel. Beams 11 (1) (2008) 014202, https://doi.org/10.1103/PhysRevSTAB.11.014202.
[18] T.J. Vink, A.R. Balkenende, R.G.F.A. Verbeek, H.A.M. van Hal, S.T. de Zwart, Materials with a high secondary-electron yield for use in plasma displays, Appl. Phys. Lett. 80 (12) (2002) 2216–2218, https://doi.org/10.1063/1.1464229.
[19] H.S. Uhm, E.H. Choi, G.S. Cho, Influence of secondary electron emission on breakdown voltage in a plasma display panel, Appl. Phys. Lett. 78 (5) (2001) 592–594, https://doi.org/10.1063/1.1343492.
[20] L. Sanche, Low-energy electron therapy, Nat. Mater. 14 (2015) 861 EP, https://doi.org/10.1038/nmat4333.
[21] D.F. Kyser, H. Niedrig, D.E. Newbury, R. Shimizu, Electron Beam Interactions with Solids for Microscopy, Microanalysis and Microlithography, Scanning Microscopy, (1982).
[22] C. Vieu, F. Carcenac, A. Pépin, Y. Chen, M. Mejias, A. Lebib, L. Manin-Ferlazzo, L. Couraud, H. Launois, Electron beam lithography: resolution limits and applications, Appl. Surf. Sci. 164 (1) (2000) 111–117, https://doi.org/10.1016/S0169-4332(00)00352-4 surface Science in Micro & Nanotechnology, http://www.sciencedirect.com/science/article/pii/S0169433200003524.
[23] R.M. Thorman, R.K.T.P.D.H. Fairbrother, O. Ingólfsson, The role of low-energy electrons in focused electron beam induced deposition: four case studies of representative precursors, Beilstein J. Nanotechnol. 6 (2017) 1904–1926.
[24] S. Luryi, Hot Electrons in Semiconductor Devices, Clarendon Press, Oxford, 1999, pp. 385–427 (Ch. 17).
[25] K. Kanaya, S. Ono, F. Ishigaki, Secondary electron emission from insulators, J. Phys. D: Appl. Phys. 11 (17) (1978) 2425.
[26] J. Cazaux, Some considerations on the secondary electron emission, δ, from e^--irradiated insulators, JAP 85 (2) (1999) 1137–1147, https://doi.org/10.1063/1.369239.
[27] W.M.E.J. Tang, A photovoltaic device structure based on internal electron emission, Nature 421 (2003) 616–618.
[28] R. Shimizu, Z. Ding, Monte carlo modelling of electron–solid interactions, Rep. Prog. Phys. 55 (1992) 487.
[29] J. Goldstein, D.E. Newbury, P. Echlin, D.C. Joy, A.D. Romig, C.E. Lyman, C. Fiori, E. Lifshin, Scanning Electron Microscopy and X-ray Microanalysis, Plenum, New York, London, 1992.
[30] L. Reimer, Scanning Electron Microscopy, Springer Verlag, Berlin Heidelberg New York, 1985.
[31] M. Kimura, M. Inokuti, M.A. Dillon, Electron degradation in molecular substances, Adv. Chem. Phys. 84 (1993) 193.
[32] K. Ueno, T. Kumihashi, K. Saiki, A. Koma, Characteristic secondary electron emission from graphite and glassy carbon surfaces, Jpn. J. Appl. Phys. 27 (5A) (1988) L759 http://stacks.iop.org/1347-4065/27/i=5A/a=L759.
[33] A. Hoffman, G.L. Nyberg, S. Prawer, High-energy angle-resolved secondary-electron emission spectroscopy of highly oriented pyrolytic graphite, J. Phys. Condens. Matter 2 (1990) 8099–8106.
[34] O.Y. Ridzel, V. Astasauskas, W.S. Werner, Low energy (1-100 ev) electron inelastic mean free path (imfp) values determined from analysis of secondary electron yields (sey) in the incident energy range of 0. 1-10 kev, J. Electron Spectrosc. Relat. Phenom. (2019), https://doi.org/10.1016/j.elspec.2019.02.003.
[35] W.S.M. Werner, Electron transport in solids for quantitative surface analysis, Surf. Interface Anal. 31 (2001) 141.
[36] U. Amaldi, A. Egidi, R. Marconero, G. Pizzella, Use of a two channeltron coincidence in a new line of research in atomic physics, Rev. Sci. Instrum. 40 (8) (1969) 1001–1004, https://doi.org/10.1063/1.1684135.
[37] R. Camilloni, A.G.G.R. Tiribelli, G. Stefani, Coincidence measurement of quasifree scattering of 9-kev electrons on k and l shells of carbon, Phys. Rev. Lett. 29 (1972) 618.
[38] D. Voreades, Secondary electron emission from thin carbon films, Surf. Sci. 60 (1976) 325.
[39] F.J. Pijper, P. Kruit, Detection of energy-selected secondary electrons in coincidence with energy-loss events in thin carbon foils, Phys. Rev. B 44 (17) (1991) 9192–9200, https://doi.org/10.1103/PhysRevB.44.9192.
[40] J. Drucker, M.R. Scheinfein, J. Liu, J. Weiss, Electron coincidence spectroscopy studies of secondary and auger electron generation mechanisms, J. Appl. Phys. 74 (1993) 7329–7339.
[41] H. Müllejans, A.L. Bleloch, A. Howie, M. Tomita, Secondary electron coincidence detection and time of flight spectroscopy, Ultramicroscopy 52 (1993) 360–368.
[42] I.E. McCarthy, E. Weigold, (e,2e) spectroscopy, Phys. Rep. 27 (6) (1976) 275–371.
[43] J. Kirschner, O.M. Artamonov, S.N. Samarin, Two-electron coincidence spectroscopy of scattering events at surfaces, Phys. Rev. Lett. 69 (1992) 1711.
[44] S. Samarin, O. Artamonov, P. Guagliardo, L. Pravica, A. Baraban, F. Schumann, J. Williams, Emission of correlated electron pairs from au(111) and cu(111)

surfaces under low-energy electron impact: Contribution of surface states, d-states and spin effects, J. Electron Spectrosc. Relat. Phenom. 198 (2015) 26–30.
[45] W.S.M. Werner, W. Smekal, H. Winter, A. Ruocco, F. Offi, S. Iacobucci, G. Stefani, Role of surface and bulk plasmon decay in secondary electron emission, Phys. Rev. B78 (2008) 233403.
[46] A. Liscio, A. Ruocco, G. Stefani, S. Iacobucci, Two-step-wise interpretation of highly asymmetric, grazing angle (e, 2e) on solids: a real momentum spectroscopy for surfaces and overlayers, Phys. Rev. B 77 (2008) 085116.
[47] W.S.M. Werner, F. Salvat-Pujol, A. Bellissimo, R. Khalid, W. Smekal, M. Novak, A. Ruocco, G. Stefani, Secondary-electron emission induced by in vacuo surface excitations near a polycrystalline al surface, Phys. Rev. B88 (2013) 201407.
[48] A. Ruocco, W.S.M. Werner, M.I. Trioni, S. Iacobucci, G. Stefani, Surface state mediated plasmon decay in al(100), Phys. Rev. B 95 (2017) 155408, https://doi.org/10.1103/PhysRevB.95.155408.
[49] K.W. Shung, Dielectric function and plasmon structure of stage-1 intercalated graphite, Phys. Rev. B34 (1986) 979.
[50] I. Schäfer, M. Schlüter, M. Skibowski, Conduction-band structure of graphite studied by combined angle-resolved inverse photoemission and target current spectroscopy, Phys. Rev. B Condens. Matter 35 (14) (1987) 7663–7670.
[51] J.B. Pendry, Low Energy Electron Diffraction, Academic Press, London, New York, 1974.
[52] R. Feder, J.B. Pendry, Theory of secondary electron emission, Solid State Commun. 26 (1978) 519.
[53] J.J.B.M.L. Xu, M.A.V. Hove, Electron scattering by atomic chains: Multiple scattering effects, Phys. Rev. 39 (1989) 8275.
[54] Y. Chen, M.A.V. Hove, C.S. Fadley, F. Bondino, R.D. Muiño, Mscd Code, (2008) http://electron.lbl.gov/mscdpack.
[55] A. Winkelmann, K. Aizel, M. Vos, Electron energy loss and diffraction of back-scattered electrons from silicon, New J. Phys. 12 (2010) 053001, https://doi.org/10.1088/1367-2630/12/5/053001.
[56] S.L. Dudarev, M.I. Ryazanov, The role of variation in the elastic cross section on multiple scattering of electrons in crystals, Soviet Phys. JETP 61 (1985) 2.
[57] S.L. Dudarev, M.J. Whelan, Temperature dependence of elastic backscattering of electrons from polycrystalline solids, Surf. Sci. 311 (1994) L687.
[58] S.L. Dudarev, P. Rez, M.J. Whelan, Theory of electron backscattering from crystals, Phys. Rev. 51 (1995) 3397.
[59] P. Schattschneider, W.S.M. Werner, Coherence in eels, J. Electron Spectrosc. Relat. Phenom. 143 (2005) 81–95.
[60] W.S.M. Werner, Electron transport in solids for quantitative surface analysis, Surf. Interface Anal. 31 (3) (2001) 141–176, https://doi.org/10.1002/sia.973.
[61] In this work we define all electron energies ≤100 ev as low-energy (le) regime and the medium-energy range going from > 100 ev up to ca. 3000 ev.
[62] B. Davison, Neutron Transport Theory, Oxford University Press, London, 1955.
[63] V.V. Sobolev, A Treatise on radiative transfer, van Nostrand, Princeton, NJ, 1963.
[64] Z.J. Ding, X.D. Tang, R. Shimizu, Monte Carlo study of secondary electron emission, JAP 89 (1) (2001) 718–726, https://doi.org/10.1063/1.1331645.
[65] R. Shimizu, D. Ze-Jun, Monte Carlo modelling of electron-solid interactions, Rep. Prog. Phys. 55 (4) (1992) 487–531, https://doi.org/10.1088/0034-4885/55/4/002.
[66] J.I. Goldstein, D.E. Newbury, J.R. Michael, N.W. Ritchie, J.H.J. Scott, D.C. Joy, Scanning Electron Microscopy and X-Ray Microanalysis, Springer New York, New York, NY, 2018, https://doi.org/10.1007/978-1-4939-6676-9.
[67] F. Salvat, A. Jablonski, C.J. Powell, ELSEPA – Dirac partial-wave calculation of elastic scattering of electrons and positrons by atoms, positive ions and molecules, Comput. Phys. Commun. 165 (2) (2005) 157–190, https://doi.org/10.1016/j.cpc.2004.09.006 https://www.sciencedirect.com/science/article/pii/S0010465504004795.
[68] B.L. Henke, E.M. Gullikson, J.C. Davis, X-ray interactions: Photoabsorption, scattering, transmission, and reflection at E = 50–30, 000 eV, Z = 1–92, At. Data Nucl. Data Tables 54 (2) (1993) 181–342, https://doi.org/10.1006/adnd.1993.1013 https://www.sciencedirect.com/science/article/pii/S0092640X83710132?via%3Dihub.
[69] E.D. Palik, Handbook of Optical Constants of Solids I& II, 1985, Academic Press, New York, 1991.
[70] J. Pierron, C. Inguimbert, M. Belhaj, M. Raine, J. Puech, Ionizing dose calculations for low energy electrons in silicon and aluminum, IEEE Trans. Nucl. Sci. 64 (2017) 2340–2348.
[71] E. Kieft, E. Bosch, Refinement of mc simulations of electron-specimen interaction in low-voltage sem, J. Appl. Phys. D 41 (2008) 215310.
[72] W.S.M. Werner, F. Salvat-Pujol, A. Bellissimo, R. Khalid, W. Smekal, M. Novák, A. Ruocco, G. Stefani, Secondary-electron emission induced by in *vacuo* surface excitations near a polycrystalline al surface, Phys. Rev. B 88 (201407(R)) (2013).
[73] V. Astašauskas, A. Bellissimo, P. Kuksa, C. Tomastik, H. Kalbe, W.S. Werner, Optical and electronic properties of amorphous silicon dioxide by single and double electron spectroscopy, J. Electron Spectrosc. Relat. Phenom. (2018), https://doi.org/10.1016/j.elspec.2019.02.008 http://www.sciencedirect.com/science/article/pii/S0368204818301993.
[74] D.R. Lide (Ed.), CRC Handbook of Chemistry and Physics, 88th Ed., CRC Press, 2008.
[75] R.E. Dunin-Borkowski, M.R. McCartney, D.J. Smith, Electron holography of nanostructured materials, Encyclopedia of Nanoscience and Nanotechnology, American Scientific Publishers, 2004, pp. 41–99.
[76] Y. Lin, D.C. Joy, A new examination of secondary electron yield data, Surf. Interface Anal. 37 (11) (2005) 895–900, https://doi.org/10.1002/sia.2107.
[77] M.S. Chung, T.E. Everhart, Simple calculation of energy distribution of low-energy secondary electrons emitted from metals under electron bombardment, JAP 45 (2) (1974) 707–709, https://doi.org/10.1063/1.1663306.
[78] P. Wallace, The band theory of graphite, Phys. Rev. 71 (1947) 622.
[79] M.S. Chung, T.E. Everhart, Role of plasmon decay in secondary electron emission in the nearly-free-electron metals. application to aluminum, Phys. Rev. B 15 (10) (1977) 4699–4715.
[80] R.C. Tatar, S. Rabii, Electronic properties of graphite: a unified theoretical study, Phys. Rev. B 25 (1982) 4126–4141, https://doi.org/10.1103/PhysRevB.25.4126.
[81] A.G. Marinopoulos, L. Reining, A. Rubio, V. Olevano, Ab initio study of the optical absorption and wave-vector-dependent dielectric response of graphite, Phys. Rev. B 69 (2004) 245419, https://doi.org/10.1103/PhysRevB.69.245419.
[82] M. Taborelli, P. Chiggiato, P. Costa Pinto, P. Cruikshank, Nine Years of Carbon Coating Development for the SPS Upgrade: Achievements and Heritage, Tech. Rep. CERN-ACC-2016-0010, CERN, Geneva, 2015https://cds.cern.ch/record/2126930.
[83] S.A. Kolomov, L.T. Chadderton, Total current spectroscopy, Surf. Sci. 90 (1979) 359–380.
[84] J.R. Rumble (Ed.), CRC Handbook of Chemistry and Physics, 99th ed., CRC Press LLC, Boca Raton, FL, 2018.
[85] J. Azoulay, et al., Photoelectron Spectroscopy: Principles and Applications, Vacuum 33 (1983) 211–213.
[86] H-Lüth, Scattering from Surfaces and Thin Films, 3rd ed., Springer, Berllin Heidelberg New York, 1995, pp. 133–212.
[87] G. Capart, Band structure calculations of low energy electron diffraction at crystal surfaces, Surf. Sci. 13 (2) (1969) 361–376, https://doi.org/10.1016/0039-6028(69)90197-6 http://www.sciencedirect.com/science/article/pii/0039602869901976.
[88] P.J. Møller, M.H. Mohamed, An experimental study of the energy dependence of the total yield due to the incidence of low- energy electrons onto graphite surfaces, JPC 15 (6) (1982) 6457–6462.
[89] V.N. Strocov, P. Blaha, H.I. Starnberg, M. Rohlfing, R. Claessen, J.-M. Debever, J.-M. Themlin, Three-dimensional unoccupied band structure of graphite: very-low-energy electron diffraction and band calculations, Phys. Rev. B 61 (2000) 4994–5001, https://doi.org/10.1103/PhysRevB.61.4994.
[90] V.N. Strocov, R. Claessen, G. Nicolay, S. Hüfner, A. Kimura, A. Harasawa, S. Shin, A. Kakizaki, H.I. Starnberg, P.O. Nilsson, P. Blaha, Three-dimensional band mapping by angle-dependent very-low-energy electron diffraction and photo-emission: methodology and application to cu, Phys. Rev. B 63 (2001) 205108, https://doi.org/10.1103/PhysRevB.63.205108.
[91] N. Barrett, E.E. Krasovskii, J.-M. Themlin, V.N. Strocov, Elastic scattering effects in the electron mean free path in a graphite overlayer studied by photoelectron spectroscopy and leed, Phys. Rev. B 71 (2005) 035427, https://doi.org/10.1103/PhysRevB.71.035427.
[92] C.Y. Vallgren, G. Arduini, J. Bauche, S. Calatroni, P. Chiggiato, K. Cornelis, P.C. Pinto, B. Henrist, E. Métral, H. Neupert, G. Rumolo, E. Shaposhnikova, M. Taborelli, Amorphous carbon coatings for the mitigation of electron cloud in the cern super proton synchrotron, Phys. Rev. Spec. Topics – Accel. Beams 14 (2011) 071001, https://doi.org/10.1103/PhysRevSTAB.14.071001.
[93] I. Bojko, N. Hilleret, C. Scheuerlein, Influence of air exposures and thermal treatments on the secondary electron yield of copper, J. Vac. Sci. Technol. A: Vac. Surf. Films 18 (3) (2000) 972–979, https://doi.org/10.1116/1.582286.
[94] A. Bellissimo, Electron Induced Secondary Electron Emission Studies of Polycrystalline Aluminium and Various Carbon Allotropes by Means of (e,2e)-Coincidence Spectroscopy, Diploma Thesis, Vienna University of Technology, 2014.
[95] V. Astašauskas, Secondary Electron-Electron Energy Loss Coincidence Spectroscopy (se2elcs) on Surfaces, Dissertation Thesis, Technische Universität Wien, 2018.
[96] A. Ruocco, M. Milani, S. Nannarone, G. Stefani, Scattering mechanism of electrons interacting with surfaces in specular reflection geometry: graphite, Phys. Rev. B 59 (20) (1999) 13359–13364.
[97] A. Bellissimo, Multiparameter Analysis of Genesis and Evolution of Secondary Electrons in the Low Energy Regime, Disseratation Thesis, Scuola Dottorale in Scienze della Materia, Nanotecnologie e Sistemi Complessi, Dipartimento di Scienze, Università degli Studi Roma Tre, 2019, https://www.researchgate.net/publication/332684398_Multiparameter_Analysis_of_Genesis_and_Evolution_of_Secondary_Electrons_produced_in_the_Low_Energy_regime.
[98] R.M. Vaughan, Secondary emission formulas, IEEE Trans. Electron Dev. 40 (4) (1993) 830, https://doi.org/10.1109/16.202798.
[99] C. Bouchard, J. Carette, The secondary electron emission coefficient of disordered surfaces, Surf. Sci. 100 (1) (1980) 241–250, https://doi.org/10.1016/0039-6028(80)90455-0.
[100] J.R.M. Vaughan, A new formula for secondary emission yield, IEEE Trans. Electron Dev. 36 (9) (1989) 1963–1967, https://doi.org/10.1109/16.34278.
[101] L.A. Gonzalez, M. Angelucci, R. Larciprete, R. Cimino, The secondary electron yield of noble metal surfaces, AIP Adv. 7 (2017) 115203.
[102] J. Cazaux, Reflectivity of very low energy electrons (< 10 ev) from solid surfaces: physical and instrumental aspects, JAP 111 (6) (2012) 064903, https://doi.org/10.1063/1.3691956.
[103] A. Dittmar-Wituski, M. Naparty, J. Skonieczny, Simple method for simultaneous measurement of work function changes and electron reflectivity variation, J. Phys. E: Sci. Instrum. 17 (12) (1984) 1139 http://stacks.iop.org/0022-3735/17/i=12/a=015.
[104] I. Bartoš, Electronic structure of crystals via vleed, Prog. Surf. Sci. 59 (1–4) (1998) 197–206.
[105] L.A. Gonzalez, R. Larciprete, R. Cimino, The effect of structural disorder on the secondary electron emission of graphite, AIP Adv. 6 (2016) 095117.
[106] E. Weigold, I.E. McCarthy, (Ian Ellery), Electron Momentum Spectroscopy, Kluwer

Academic/Plenum Publishers, New York, 1999, pp. 253–261 includes bibliographical references and index.
[107] G. Stefani, M.V. Marabello, L. Avaldi, R. Camilloni, Does Asymmetric (e,2e) Approach the Dipolar Limit at Intermediate Energies? Vol. 414 of NATO ASI Series (Series C: Mathematical and Physical Sciences), Springer, Dordrecht, 1993.
[108] I.E. McCarthy, Range of validity of distorted wave born and impulse approximations for (e,2e), Zeitschrift für Physik D Atoms, Mol. Clust. 23 (4) (1992) 287–293, https://doi.org/10.1007/BF01429249.
[109] M. Vos, I.E. McCarthy, Observing electron motion in solids, Rev. Mod. Phys. 67 (1995) 713–723, https://doi.org/10.1103/RevModPhys.67.713.
[110] S. Rioual, S. Iacobucci, A.S.K.D. Neri, G. Stefani, Momentum distribution and valence-band reconstruction in graphite by grazing incidence (*e*, 2*e*) spectroscopy, Phys. Rev. B 57 (1998) 2545–2549, https://doi.org/10.1103/PhysRevB.57.2545.
[111] A.S. Kheifets, M. Vos, Spectral electron momentum density calculations in graphite, J. Phys. -Condens. Matter 7 (1999) 3895–3904, https://doi.org/10.1088/0953-8984/7/20/009.
[112] J. Kirschner, O.M. Artamonov, S.N. Samarin, Angle resolved energy correlated coincidence electron spectroscopy of solid surfaces, Phys. Rev. Lett. 75 (12) (1995) 2424–2427.
[113] S. Iacobucci, A. Ruocco, S. Rioual, M. Mastropietro, G. Stefani, Fully resolved kinematics of grazing-incidence (e,2e) experiments, Surf. Sci. 454–456 (2000) 1026.
[114] A.S. Kheifets, S. Iacobucci, A. Ruocco, R. Camilloni, G. Stefani, Mechanism of the low-ejection-energy (e,2e) reaction on a graphite surface, Phys. Rev. B 57 (12) (1998), https://doi.org/10.1103/PhysRevB.57.7360.
[115] E.H. Hwang, S.D. Sarma, Dielectric Function, Screening, and Plasmons in 2d Graphene, (2008) arXiv 0 (0610561v3).
[116] J. Berakdar, M.P. Das, Electron ejection from clean metallic surfaces upon charged particle impact, Phys. Rev. A 56 (1997) 1403–1413, https://doi.org/10.1103/PhysRevA.56.1403.
[117] U. Diebold, A. Preisinger, P. Schattschneider, P. Varga, Angle resolved electron energy loss spectroscopy on graphite, Surf. Sci SS (197) (1987) 430–443.
[118] S. Iacobucci, P. Letardi, M. Montagnoli, P. Nataletti, G. Stefani, An angular resolved electron energy loss investigation of highly oriented pyrolitic graphite electronic structure, J. Electron Spectrosc. Relat. Phenom. 67 (3) (1994) 479–488, https://doi.org/10.1016/0368-2048(93)02033-I http://www.sciencedirect.com/science/article/pii/036820489302033I.
[119] D.D.L. Chung, Review graphite, J. Mater. Sci. 37 (2002) 1–15.
[120] A. Bellissimo, Software for Planning and Evaluating an (e,2e)-Coincidence Experiment, Tech. Rep. Università degli Studi Roma Tre, Dipartimento di Scienze, 2017.